https://doi.org/10.5194/wes-2025-114
Preprint. Discussion started: 14 July 2025

WIND ENERGY SCIENCE DISCUSSIONS

Modelling of wind flows over realistic forests with LES

Hugo Olivares-Espinosa and Johan Arnqvist

Department of Earth Sciences, Uppsala University, Visby, Sweden

Correspondence: Hugo Olivares-Espinosa (hugo.olivares@geo.uu.se)

Abstract.

An LES based model for the simulation of wind flows over realistic forests and topography is presented. Terrain elevation as well as forest density maps from airborne laser scans are employed to investigate the importance of specific model choices related to capturing upstream terrain effects on the wind resource. The study is divided in three parts. Firstly, an extended verification process over idealized conditions is carried out. Secondly, a validation where the model is compared to field measurements acquired in the south-east of Sweden and finally an assessment of the forest and terrain footprint based on variations of the surface representation. The results show an agreement of turbulence statistics compared to the literature when forest is explicitly modelled, following expected trends as a function of the tree density. When the forest is explicitly modelled the impact of the ground roughness becomes insignificant, even for an unrealistically sparse forest. The study also demonstrates that a model relying only on ground roughness yields notable differences in the turbulence characteristics. This is partly attributed to the inability of the model to reproduce sufficient drag for forest-equivalent values of roughness length z_0 while maintaining the applicability of wall functions, which can impose strict limitations on the grid near ground. This is further complicated by the problem of converting realistic, heterogeneous forests fields to z_0. Moreover, turbulence statistics in the roughness sublayer are affected by the lack of vertical permeability. The validation shows that the model is able to capture the flow characteristics imprinted by different surface features on the wind along three distinctive wind directions. Vertically separated spectral coherence from the LES is slightly below compared to the IEC standard, which can be attributed to the reference velocities used in the normalization of the frequency. The footprint study shows that the heterogeneity of a realistic forest produces higher drag in comparison with homogeneous conditions while also providing a better agreement with observations. An analysis based on correlations of upstream forest drag with target wind statistics shows that a point above the terrain is most significantly influenced by the footprint of a forest area located at about 10 times upstream of its height above ground. When correlations are applied to turbulence, this separation increases five-fold. These findings provide a valuable insight to determine the optimal domain size of a computational domain in forest simulations under neutral atmospheric stratification. Further comparisons of fully uniform vs. limited areas of realistic forest revealed that at heights above 100 m no clear differences in the wind flow are seen. Conversely, comparing flat terrain with the actual topography –with a realistic forest distribution on both cases– demonstrated a clear importance of capturing small scale terrain features.

https://doi.org/10.5194/wes-2025-114
Preprint. Discussion started: 14 July 2025

WIND ENERGY SCIENCE DISCUSSIONS

1 Introduction

The expansion of wind energy has lead to an increasing interest in the development of projects over remote locations that offer conditions far from the flat and obstacle-free considered as ideal. Forested regions are of interest due to reasons such as the reduced social opposition and the concurrent interests with forestry to share costs for access roads and management. Conversely, they present some of the most challenging wind conditions for the operation of wind turbines: the wind speed is lower, with a stronger vertical shear and higher turbulence intensity compared to winds over terrain with lower vegetation. Indeed, in forested locations wind turbines require more maintenance (Zendehbad et al., 2016). The study of wind flows above forests is far from being restricted to the wind energy community, on the contrary, it is highly relevant in investigations concerning any other structure found on such regions that is subjected to large dynamic loads, such as buildings or bridges, as well as decidedly important in forestry and agricultural applications (Niklas, 1985; Gardiner, 1994; Schindler et al., 2012).

Wind flow over forested terrains differs in some aspects compared to that over terrains free of vegetation. The former carries large coherent structures that penetrate the canopy and dominate the turbulence dynamics, including momentum fluxes as well as scalar transport.In some aspects the description of a canopy flow fits more that of a mixing-layer than a boundary layer, an analogy first made by Raupach et al. (1996). This is revealed by the distinctive inflection point in the velocity profile at the canopy top as well as other contrasting features to those of a surface layer flow, such as variations in high-order statistical moments, the growth pattern of the turbulence lengthscales or the relations between sweeps and ejections, defined by the directions of components of the shear stress (Gardiner, 1994). The main characteristics of canopy turbulence, gathered from experimental field campaigns and wind tunnel data, were depicted by Raupach et al. (1996) in figures they called a “family portrait", providing a quick reference for the turbulence characteristics for varying canopy heights and densities. These figures have since then been reproduced and complemented by other authors, for instance, Brunet (2020). The effect of the forest in this roughness sublayer is conventionally assumed to extend vertically to $z \approx 2 \sim 3$ times the forest height h.Above it, the wind profile recovers its near logarithmic shape with height $z-d$, where d is the zero plane displacement height, identified by Thom (1971) and later Jackson (1981) as the level at which the mean drag appears to act on the flow. The asymptotic transition to turbulence statistics similar to those over low vegetation at $z \approx 2 \sim 3h$ is also supported by measurements over real forests (Arnqvist et al., 2015, 2024).

A relevant problem when modelling flows over high roughness at high resolution is that the first grid node above ground ends up embedded deep within the roughness sublayer, where usual flux-gradient expressions are invalid (Basu and Lacser, 2017). Since the roughness sublayer is estimated to be two to three tree heights deep, this problems will be present for microscale simulations of all natural forests. While solutions do exist, they come with unfavourable compromises like setting the height of the first cell undesirably high or moving the stress boundary condition several grid cells up vertically.

The first usage of a second-order closure to model canopy flow was made by Wilson and Shaw (1977) whose 1D formulation includes also a separate source term to account for the forest drag —that has become ubiquitous in CFD studies of canopy flows (see eq. (16)), have been shown able to predict second-order features when comparing with tower measurements (Brunet, 2020). Svensson and Häggkvist (1990) show an early example of employing source terms in the two-equation $k-\varepsilon$ formulation for

https://doi.org/10.5194/wes-2025-114
Preprint. Discussion started: 14 July 2025

canopy flows (where k is the Turbulence Kinetic Energy or TKE and ε is the turbulence dissipation). As it is inherent to Reynolds-Averaged Navier-Stokes (RANS), a significant challenge is the determination of the modelling coefficients, perhaps even more so in the case of the canopy. This process can involve the usage of other CFD, such as Silva Lopes et al. (2013) or experimental measurements. Among the latter, the model and constants of Sogachev and Panferov (2006) has been favourably used to model wind over heterogeneous forest distributions (Ivanell et al., 2018) and has been later extended (Sogachev, 2009; Sogachev et al., 2012) for the modelling transient atmospheric stability, most suitable for Unsteady RANS (URANS) calculations as in Sanz Rodrigo et al. (2017, 2021).

In spite of these advances, some of the turbulent flow is characterized by transient coherent eddy structures that are beyond the capabilities of RANS as statistical closure models cannot distinguish between these and incoherent structures (Brunet, 2020). Canopy flows also display distinct features such as sweeps and ejections (downward and upward moving gusts, respectively), that dominate the turbulence transfer of momentum, heat and mass between the canopy and the atmosphere (Gardiner, 1994; Dupont and Brunet, 2009). Consequently, a faithful representation of the wind dynamics on forested regions requires a modelling technique able to represent the relevant spatial and transient features of these eddy structures. Large-Eddy Simulation (LES) has proven a suitable technique for the reproduction of wind turbulence since larger scales that dominate the flow dynamics are fully resolved, therefore explicitly representing the most significant motions.

While LES has an extensive use in modelling ABL flows over rough terrains, adjustments to the model equations are required in the case of vegetation canopies. Next to the forest drag acting on the filtered scales, the wakes of leaves and branches precipitate the dissipation of turbulence with respect to the normal breakup of eddies along the energy cascade, an effect sometimes referred to as a “short circuit” of the cascade process (Ayotte et al., 1999) or “spectral short cut” (Finnigan, 2000; Finnigan et al., 2009). This signifies a transfer of energy from the mean flow to the subgrid scales which requires the addition of an extra term in the Sub-Grid Scale (SGS) energy budget (Shaw and Patton, 2003).

Since the first LES study of homogeneous canopies by Shaw and Schumann (1992) making usage of an explicit forest drag, multiple studies have continue using this method to model canopy flows. This approach permits, in the first instance, to investigate the characteristics of various statistical moments (Su et al., 1998), carry out one- or two-point correlations and investigate the spectral features of turbulence over forests (Su et al., 2000). LES has shown to be a convenient tool for the study of coherent turbulence structures over canopies, e.g. Finnigan et al. (2009), Gavrilov et al. (2011, 2013); Aumond et al. (2013), Bailey and Stoll (2016) and Arnqvist et al. (2024). Investigations about the role of these structures in the processes of turbulent transport within and above canopies are frequently carried out using Quadrant-Hole (QH) analysis technique (Lu and Willmarth, 1973) to identify sweeps and ejections, e.g. Finnigan et al. (2009), Dupont and Brunet (2009), Gavrilov et al. (2011) and Bailey and Stoll (2016). A topic of considerable interest has been the effect of variations in forest density (Dwyer et al., 1997; Dupont and Brunet, 2008a; Adedipe et al., 2020) as well as discontinuities (Silva Lopes et al., 2015; Bou-Zeid et al., 2020) and forest edges (Dupont and Brunet, 2008b, 2009; Boudreault et al., 2017). As pointed out by Bou-Zeid et al. (2020) it has been challenging to develop a clear and coherent theoretical framework that encompasses all of the relevant physics involved in flow over heterogeneous surfaces, particularly when the heterogeneity is less structured.

https://doi.org/10.5194/wes-2025-114
Preprint. Discussion started: 14 July 2025

eawe european academy of wind energy
Open Access WIND ENERGY SCIENCE DISCUSSIONS

The advent of Airborne Laser Scans (ALS) has opened new avenues in the field, allowing for an enhanced representation of realistic forests. The point cloud data, consisting of reflections from laser pulses on the ground as well as tree trunks, branches and leaves, are used to create terrain elevation maps as well as to calculate Plant Area Density (PAD) fields and Plant Area Index (PAI) of a desired area (Boudreault et al., 2015; Arnqvist et al., 2020). The utilization of detailed PAD maps in LES provides a significant advantage compared to conventional methods where variations in forest density are represented by modifying an a priori assumed density profile (Dwyer et al., 1997; Dupont and Brunet, 2008a). Even if only information of the forest height is used, the detail in the ALS data has been shown to lead to significantly better wind resource estimation compared to surface descriptions with less detail and accuracy Floors et al. (2018). Examples of studies that have made use of ALS-derived PAD maps are Boudreault et al. (2017); Ivanell et al. (2018), Olivares-Espinosa et al. (2019), Abedi et al. (2021) and Arnqvist et al. (2024), permitting the study of high-order turbulence statistics from realistic forest setups. A particular benefit of using ALS derived PAD fields is the capability to represent the effects of features of the ground and forest heterogeneities along an upstream fetch on the wind profiles at a particular location, an attribute referred to as footprint. This aspect has been show in Ivanell et al. (2018) and Arnqvist et al. (2019) where the usage of PAD fields in LES enables to reproduce properties in the wind profile hypothesized to stem from characteristics in the footprint of different incoming wind directions. The question of how large such an upstream region needs to be is partly the subject of the present work.

An additional benefit of using PAD fields in numerical simulations is that variations in tree height as well as clearings are directly incorporated and their subsequent effect in the canopy shear stress is naturally assimilated. Indeed, as shown by Silva Lopes et al. (2015) and Janzon et al. (2023), landscapes of alternating forests and clearings yield a shear stress that in average is larger than the sum of the equilibrium stresses over homogeneous patches, resulting in a higher effective z_0. On the contrary, Boudreault et al. (2017) found using RANS that the horizontal heterogeneities induce higher turbulence predominately at the canopy top while decreasing the displacement height that in turn leads to higher velocities compared to a homogeneous canopy. While the literature thus is conflicting on the impact of heterogeneous forest cover on the wind above, it is clear that to represent a real forest with constant tree height and homogeneous density profile is a crude approximation.

For wind power deployment in forested landscapes, the main focus is on shear and turbulence magnitude, with directional shear, integral lengthscales and other turbulence statistics also being of interest (Robertson et al., 2019). As it is still an open question what methodology is suitable to predict such properties in the wind given a specific site, this work scrutinize the use of realistic PAD profiles in LES and investigates to which extent its use can improve predictions of wind statistics owing to the character of the upstream forest footprint.

The layout of this work is as follows: First, the requirements to reach statistically significant conclusions are examined, followed by a description of the field measurements, the flow model and the post-processing of the data. This is followed by the results, divided in 3 parts: first with focus on the verification of the PAD approach, then the validation against field measurements and finally with respect to the impact of the upstream forest cover. The paper finishes with conclusions of the most important findings for each of these parts as well as recommendations and reflections regarding future research on the topic.

https://doi.org/10.5194/wes-2025-114
Preprint. Discussion started: 14 July 2025

2 Assessment of requirements to test site specific CFD capability

The following section presents a brief outline of the statistical requirements for numerical simulations that permit to establish whether differences in results arise due to distinct upstream conditions rather than stochastic variability. The aim of this is to confirm that the modelling technique is able to reproduce differences owed to surface heterogeneities.

2.1 Requirements on the length of the LES run

The inclusion of the physical mechanisms into an LES model required to reproduce its response to the boundary conditions representing a particular site (PAD and topography in the present case) does not guarantee by itself the capability of reproducing the wind flow with a reasonable precision. Additional requirements are necessary regarding the accuracy of the validation measurements, boundary conditions and wind statistics. Even under the assumption of an accurate measurement of the parameters employed to define the boundary conditions as well as wind statistics (or within a negligible error), the statistical uncertainty of the LES simulation itself must be such that any random error is smaller than the site specific response in the wind statistics. According to Lumley and Panofsky (1964) the statistical uncertainty for wind speed can be estimated by

$$\frac{\sigma_{\overline{u}}}{\overline{u}} = \left(\frac{2\mathcal{T}_1\sigma_u^2}{T\overline{u}^2}\right)^{1/2}, \tag{1}$$

where $\overline{u}$ is the mean wind, $\sigma_{\overline{u}}$ is the random error of the mean wind, $\mathcal{T}_1$ is the integral time scale of u, σ_u^2 is the variance of the instantaneous streamwise wind and T is the length of the simulated time series. An estimation of the magnitude of the relative random error can be made by assuming that $\mathcal{T}_1 \sim 10z/\overline{u}$, where z is the height above ground, and $\sigma_u^2/U^2 \sim 10^{-2}$. Assuming $z/\overline{u} \sim 10$ implies that it would be necessary to simulate at least 20000 s to get below a relative random error of 1%.

The relative random error for second order moments can, according to Lenschow et al. (1994), be estimated by

$$\frac{\sigma_{\overline{u_i u_j}}}{\overline{u_i' u_j'}} = \left(\frac{2\mathcal{T}_{ij}}{T}\right)^{1/2}, \tag{2}$$

where $\mathcal{T}_{ij}$ is the integral time scale of the second order moment. Assuming again that $\mathcal{T}_{ij} \sim 10z/\overline{u}$ implies that the relative random error for $\overline{u_i' u_j'}$ is 10 % at 100 m height for a simulation of length 20000 s. To get to a relative random error below 1 % would require to simulate 2×10^6 s, or more than 23 days of physical time!

Using scaling arguments, a relative difference in mean wind between two different wind directions at a single site due to different surface roughness can be estimated. For wind speed we have that

$$\frac{\overline{u}}{u_*} = \frac{1}{\kappa}\ln z/z_0, \tag{3}$$

where u_* is the friction velocity, κ is the von Kármán constant and z_0 is the roughness length. Taking the difference between two directions (direction 1 and 2) we get

$$\Delta\overline{u} = u_{*_1}\frac{1}{\kappa}\ln z/z_{0_1} - u_{*_2}\frac{1}{\kappa}\ln z/z_{0_2}. \tag{4}$$

Furthermore, if the difference in roughness lengths between the two directions is relatively small, the ratio of roughness lengths between the two directions is much larger than the ratio in wind speed or friction velocity so that the latter two ratios can be approximated to 1. This allows to extract $\overline{u}$ from the right hand side:

$$\frac{\Delta\overline{u}}{\overline{u}} \approx \frac{\ln z_{0_2}/z_{0_1}}{\ln z/\overline{z_0}}, \tag{5}$$

where $\overline{z_0}$ is the mean roughness length of the two directions. To provide an example, if one direction has a fetch with a roughness length of 2 m and another direction has a roughness length of 1.5 m, the relative wind speed difference between them at 100 m height would be approximately 7 % according to eq. (5).

Using the logarithmic law, eq. (3), we can also estimate the relative difference in shear stress owing to a (small) difference in z_0:

$$\Delta u_*^2 = \left(\frac{\kappa\overline{u_1}}{\ln z/z_{0_1}}\right)^2 - \left(\frac{\kappa\overline{u_2}}{\ln z/z_{0_2}}\right)^2. \tag{6}$$

Assuming that we want to estimate the difference in u_*^2 for a fixed wind speed at height z, and assuming we can approximate the mean shear stress as $[\kappa\overline{u}/\ln(z/\overline{z_0})]^2$ we get the following expression for the relative difference in shear stress,

$$\frac{\Delta u_*^2}{\overline{u_*^2}} \approx \ln(z/\overline{z_0})^2\left(\frac{1}{\ln(z/z_{0_1})^2} - \frac{1}{\ln(z/z_{0_2})^2}\right). \tag{7}$$

This expression indicates that at 100 m height, we can expect a relative difference in the shear stress of 14 % between a direction with $z_0 = 2$ m compared to a direction with $z_0 = 1.5$ m.

From the above estimations we can conclude that it is reasonable to expect of a LES model that has simulated 20000 s physical time to reproduce differences in mean wind speeds between two different wind directions at a particular site, but that validating the models' ability to detect differences in higher order statistics would be on the limit of statistical uncertainty.

2.2 Requirements on the length of the model domain

In order to roughly estimate the requirements on domain size to capture the footprint of a heterogeneous terrain we apply the following scaling arguments: if there is a heterogeneity in the wind field owing to a heterogeneity in the surface roughness or topography, its local impact on the streamwise wind can be estimated by the size of the streamwise advection term in the momentum equation,

$$\overline{u}\frac{\partial\overline{u}}{\partial x} \sim \overline{u}\frac{\Delta\overline{u}}{x}. \tag{8}$$

On the other hand, the most important term that tends to even out heterogeneity in the wind field is the vertical shear stress divergence,

$$\frac{\partial\overline{u'w'}}{\partial z} \sim \frac{u_*^2}{z}. \tag{9}$$

Assuming both $\Delta\overline{u}$ and u_* are of the order $0.1\overline{u}$ we can estimate the ratio between the strength of the advection term to the shear stress divergence as

$$\frac{\overline{u}z}{u_*x} \sim \frac{10z}{x}. \tag{10}$$

https://doi.org/10.5194/wes-2025-114
Preprint. Discussion started: 14 July 2025

eawe european academy of wind energy
Open Access WIND ENERGY SCIENCE DISCUSSIONS

For upstream distances shorter than $10z$ the advection will dominate and the wind field will be characterized the upstream heterogeneity. On the other hand, if advection is to be completely negligible, either the upstream surface conditions must be homogeneous or the distance x to the heterogeneity must satisfy $x \gg 10z$. To quantify, we expect that an upstream heterogeneity lying further away than $100z$ would contribute with less than 10 % of the momentum balance of the flow. Thus, we conclude that to capture most of the effects from an upstream surface heterogeneity, the model domain should extend downstream roughly 100 times the highest height of the wind turbine rotor.

3 Site description and measurements

3.1 Site description and surface data

Metmast measurements correspond to an experimental campaign at the location of Ryningsnäs, a forested and mildly complex region in the southern part of Sweden, at about 30 km from the coast of the Baltic sea.

While part of the simulation cases in this work assume idealized forest conditions, LES are also produced to represent on-site conditions whose results are compared to measurements. Following Ivanell et al. (2018); Arnqvist et al. (2019), three different wind directions were modelled in order to see if the impact of the upstream vegetation cover is the same in the LES as in the observations. The different cases are summarized in Table 3. While all cases have predominately forest cover upstream for at least 30 km, surface characteristics vary for the three incoming wind directions: case R1 is characterized by a 400 m wide clearing just upstream of the met tower, case R2 has a valley covered with low vegetation (crops) dominating the fetch between 5 and 10 km upstream while case R3 is impacted by the same valley, but to much lesser degree and as such has less distinct features in its fetch.

The characterization of the surface data was made by analyzing point clouds from ALS with the method of Arnqvist et al. (2020). The point cloud was used to compute PAD, ground height and vegetation height in a 10 m $\times$10 m grid. The vertical resolution of the PAD data was 1 m. Detailed descriptions of the vegetation cover in the three directions are given in Ivanell et al. (2018).

3.2 Measurements

The measurements were taken from a 140 m high met tower operated between 2009 and 2012. The instrumentation consisted of 6 Metek USA-1 3D-sonics and 7 Thies first class cup anemometers. The measurement heights were 40, 59, 80, 98, 120, and 137.7 m for the sonics and 25.5, 40.1, 60.5, 80.1, 95.85, 120.75, and 137.6 m for the cups. More details of the measurements can be found in Arnqvist et al. (2015) and Bergström et al. (2013).

3.2.1 Statistical processing

For wind speed the average between the cup anemometers and the sonic anemometers was used. The shear exponent of the power law for the wind speed was calculated between two height levels in the tower as

https://doi.org/10.5194/wes-2025-114
Preprint. Discussion started: 14 July 2025

$$\alpha = \frac{\ln(\overline{u_u}/\overline{u_l})}{\ln(z_u/z_l)}, \tag{11}$$

where $\overline{u_u}$ and z_u is the mean wind speed at the upper level and $\overline{u_l}$ and z_l is the mean wind speed and height of the lower level. The height where α is valid was calculated as the mean of z_u and z_l.

In order to filter out neutral conditions the Obukhov length was used;

$$L = -\frac{\theta_0 u_*^3}{\kappa g \overline{w't'}}, \tag{12}$$

where $u_* = (\overline{u'w'}^2 + \overline{v'w'}^2)^{1/4}$ is the mean friction velocity, θ_0 the mean temperature, κ=0.4 is the von Kármán constant, g is the gravitational acceleration and $\overline{w't'}$ is the kinematic temperature flux from the vertical velocity and the fluctuating virtual temperature as measured by the sonic anemometer. For the definition of the friction velocity and the Obukhov length the height 40 m was used, reflecting a desire to avoid roughness sublayer effects while still being relatively close to the surface.

To provide validation data for the LES, the same filtering as in Ivanell et al. (2018) was used. Data was selected for wind speeds between 7 m/s and 8 m/s at 98 m height and the ratio $(z-d)/L$, where z is the height above the surface and d is the displacement height, within the range -0.1 to 0.07 at all heights (allowing for approximately $\pm$ 35 % deviation from 1 of the non-dimensional wind gradient according to the formulation by Högström, 1996). Long term averages were then constructed by averaging all 30 minute mean values satisfying the filtering criteria.

4 Flow model

4.1 Model description

A methodology to simulate the wind flow over forested and complex terrains has been implement on the OpenFOAM platform v.3.0.1 (Weller et al., 1998; Greenshields, 2015). This is based on LES of an incompressible and neutrally stable atmosphere where the SGS turbulence is modelled via a transport equation for k_{SGS}, the subgrid TKE (Yoshizawa and Horiuti, 1985; Yoshizawa, 1986) to yield an estimation of ν_{SGS}. Following the notation of $\widetilde{\cdot}$ for the filtered quantities, the equation reads

$$\frac{\partial k_{\text{SGS}}}{\partial t} + \frac{\partial \widetilde{u}_j k_{\text{SGS}}}{\partial x_j} = -\tau_{ij}\widetilde{S}_{ij} - C_\epsilon \frac{k_{\text{SGS}}^{3/2}}{\Delta} + \frac{\partial}{\partial x_j}\left[(\nu + \nu_{\text{SGS}})\frac{\partial k_{\text{SGS}}}{\partial x_j}\right] + \varepsilon_{\text{SGS},f}\ , \tag{13}$$

where $\widetilde{S}_{ij}$ is the rate-of-strain tensor and τ_{ij} the subgrid stress tensor, approximated as in other eddy-viscosity based SGS models (Pope, 2000). The subgrid viscosity is then computed as

$$\nu_{\text{SGS}} = C_k \sqrt{k_{\text{SGS}}}\Delta \tag{14}$$

where Δ corresponds to the filter size that for the implicit filtering used in our computations, corresponds to the local cell length $\Delta = (\Delta_x \Delta_y \Delta_z)^{1/3}$. The constants in the previous equations are set to $C_\epsilon = 1.048$ and $C_k = 0.094$. The last term of

https://doi.org/10.5194/wes-2025-114
Preprint. Discussion started: 14 July 2025

WIND ENERGY SCIENCE DISCUSSIONS

eq. (13) is an additional quantity that represents the contribution to the subgrid dissipation due to the wakes of the canopy elements, following Shaw and Patton (2003), it is modelled as:

$$\varepsilon_{\mathrm{SGS},f} = -\frac{8}{3} C_{\mathrm{D}} a \, |\widetilde{\boldsymbol{u}}| \, k_{\mathrm{SGS}} \tag{15}$$

In the resolved scales of the LES, the forest is represented as a source term $F_{\mathrm{D},i}$ in the momentum equation, acting as drag force in the x_i-direction (Shaw and Schumann, 1992):

$$F_{\mathrm{D},i} = -C_{\mathrm{D}} a \, |\widetilde{\boldsymbol{u}}| \, \widetilde{u}_i \ , \tag{16}$$

where a is the frontal leaf area density, assumed to be equal to PAD. A constant value of $C_{\mathrm{D}} = 0.2$ is employed for the drag coefficient for the forest.

The effect of the terrain roughness is considered via a wall model in the LES. For this, the wall model implementation found within the libraries of SOWFA (Churchfield et al., 2014) is employed. This corresponds to the model of Schumann (1975) where the velocity deficit due to the ground is represented by means of a surface stress. For this, the non-zero components of the surface stress-tensor are calculated based on the friction velocity, which in turn is computed from the assumption of a logarithmic profile.

4.2 Numerical setup

Three distinct numerical setups are employed for the different groups of simulations performed in this work. According to the purpose, these can be listed as follows:

1. A setup employed for a verification study of the wall and forest modelling. The ground is flat, with a forest simulated as uniformly dense with a constant height. This mesh has the finest resolution compared to the remaining setups.
2. A setup dedicated to simulate the wind characteristics at Ryningsnäs and reproduce the measurements described in Sec. 3. There are 3 meshes for this setup, one for each wind direction, representing the topography and tree density distribution of the location.
3. A setup to investigate the footprint of the surface features on the wind, by modifying the extension of the forest and topography heterogeneities within the computational domain.

The flow is driven by means of a forcing term in the LES momentum equation equal to the pressure gradient yielded from the given geostrophic vector $\boldsymbol{u}_g$. Simulations include a Coriolis force corresponding to 45°N for the setup 1 and to the location of Ryningsnäs, at latitude of 57°N, for setups 2 and 3. The details of the numerical setups are described in the following sections.

4.2.1 Numerical setup 1: verification cases

The mesh consists of a square box with longitudinal, crosswise and vertical dimensions of $\mathrm{L}_x \times \mathrm{L}_y \times \mathrm{L}_z = 3H \times 3H \times H$ with $H = 1280$ m. In the horizontal plane, cells are uniformly distributed with $N_x \times N_y = 548 \times 548$ cells yielding a resolution

https://doi.org/10.5194/wes-2025-114
Preprint. Discussion started: 14 July 2025

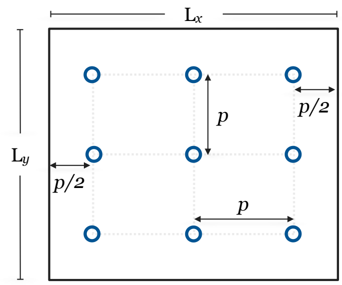

Figure 1. Layout of the sampling positions over the horizontal plane of the domain for the setup 1, Sec. 4.2.1. The circles represent the positions of the 9 vertical lines where the velocity is sampled at every cell centre. The lines are evenly separated by a distance $p = H$.

of $\Delta_x = \Delta_y \approx 7$ m. In the vertical direction, the mesh is constructed like this: a uniform mesh resolution of $\Delta_z = 5$ m up to $z = 130$ m, above this height cells are stretched at a rate of ≈ 1.037. The mesh is then vertically refined by halving the cell height in two subsequent steps: first within the region of cells below $z = 80$ m and then once more for all cells below $z = 40$ m. This yields a vertical cell resolution of $\Delta_z = 1.25$ m below 40 m –within and above the forest–, $\Delta_z = 2.5$ m between 40 m $\leq z \leq$ 80 m and $\Delta_z = 5$ m between 80 m $\leq z \leq$ 130 m and a total of $N_z = 116$ cells, for a total of $N \approx 35.8 \times 10^6$ cells. A slight modification to the vertical zone covered by the second refinement was needed for the cases with larger roughness lengths ($z_0 = 0.5$ m and 0.65 m) to avoid that it would get close to the height of the first node, i.e. to prevent $z_1 = \Delta_{z,1}/2 \approx z_0$. In those cases —to be described in Sec. 6.1—, the second refinement starts at $z = 2.5$ m instead of $z = 0$. All the lateral boundaries are set to periodic whereas the top boundary is a symmetry plane. The flow is driven by a pressure gradient with a fixed geostrophic wind of $u_g = 9$ m/s in the longitudinal direction (equivalent to $\varphi = 270$ deg). Simulations are first run over a domain with a mesh without the 2 vertical refinements process (so $\Delta_z = 5$ m is maintained up to $z = 130$ m) and $z_0 = 0.03$ m during 320×10^3 s. The resulting fields are then interpolated onto the vertically-refined mesh, where simulation is run for an additional 120×10^3 s employing the modelling features of the given verification case. These runs employ a varying time-step Δt calculated as to maintain a domain maximum Courant-Friedrichs-Lewy number of CFL$\lesssim 0.85$. Considering that the simulations yield a velocity magnitude of approximately 5 m/s at 100 m, this period is equivalent to about 156 longitudinal flow-through times (LFTT). Convergence of 4th-order moments of velocity at heights up to 500 m is observed during this period. Lastly, simulations are run with a fixed $\Delta t = 0.14$ s during 20×10^3 s to gather velocity time-series and average fields for sampling (26 LFTT). The latter is carried out along vertical lines arranged in a layout as shown in Fig. 1. u_i is sampled at every cell centre along each of the 9 columns.

4.2.2 Numerical setup 2: Ryningsnäs simulations

Three different domains are used, with the longitudinal direction L_x aligned with each incoming wind direction φ. For every case the domains are square boxes of $L_x \times L_y \times L_z = 32$ km $\times$ 20 km$\times \sim 1.2$ km. The metmast is located at $d_{MM} = 20$ km in the longitudinal direction, in the middle of the spanwise plane. The mesh is constructed with 3 regions of different resolutions

https://doi.org/10.5194/wes-2025-114
Preprint. Discussion started: 14 July 2025

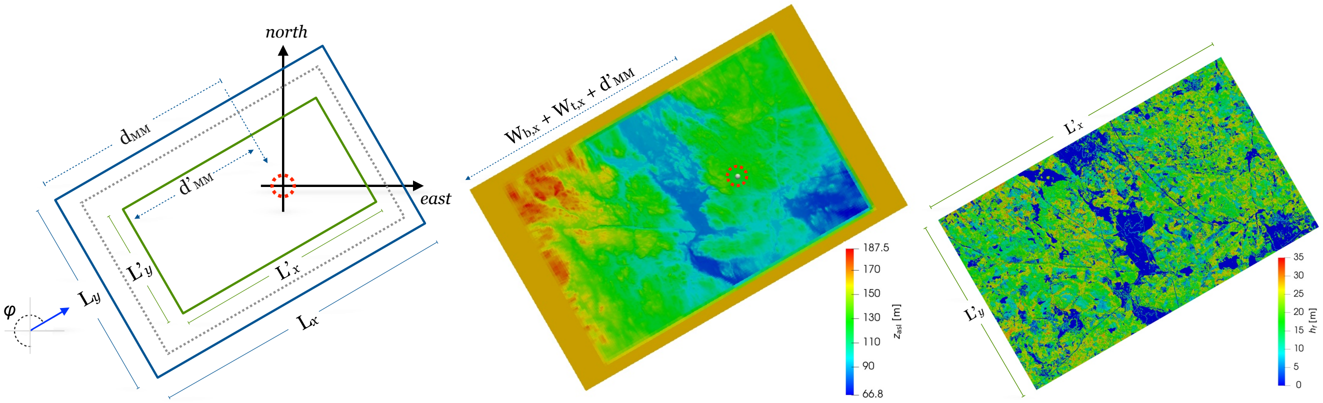

Figure 2. Computational domain in the horizontal plane employed for the Ryningsnäs simulations, as described in sections 4.2.2 and 4.2.3. The dashed circle denotes the location of the metmast. *Left:* dimensions of the domain and the farm region (prime labels). *Middle:* terrain elevation, labels indicate the extensions of the different mesh sections with respect to the metmast location. *Right:* tree height within the farm region. All images correspond to the 240° wind direction case.

in the horizontal plane referred to as *farm* where resolution is highest, *buffer* with coarse cells at the outer edge of domain and *transition* where cells stretch in between the to former regions. A top view of the computational domain is presented in Fig. 2 (left) showing the innermost farm region $\mathrm{L}'_x \times \mathrm{L}'_y = 20\ \mathrm{km} \times 12\ \mathrm{km}$, the transition —between the farm and the dashed rectangle—, the buffer region —the edge outwards from the dashed rectangle— and the overall horizontal dimensions of the domain $\mathrm{L}_x \times \mathrm{L}_y$. The widths of the transition and buffer edge regions in the longitudinal and spanwise directions are $\mathrm{W}_{t,x} = 3$ km, $\mathrm{W}_{t,y} = 2.5$ km and $\mathrm{W}_{b,x} = 3$ km, $\mathrm{W}_{b,y} = 1.5$ km, respectively. Fig. 2 (right) shows the horizontal plane of the 240° case with a color scale corresponding to the terrain elevation, also indicating the distance to the metmast d_{MM} as the sum of the widths of the buffer, transition and the $\mathrm{d}'_{\mathrm{MM}} = 14$ km (location of metmast from the edge of the farm region). As shown in the figure, the elevation becomes flat within the inmost 500 m buffer so the elevation is equal at the outermost boundary, corresponding to 63.06 m above sea level (100° case), 163.25 m above sea level (240°) and 137.76 m above sea level (290°). The horizontal cell resolution in the farm region is $\Delta_x = \Delta_y = 25$ m (squared cells), stretching towards the buffer region where cells are also squared with 250 m per side. The height of the first cell Δ_{z_1} at the metmast location is about 3.4 m in all cases, with cells stretching in the vertical direction at uniform rate of approximately 1.05 . The variations in elevation in the terrain covered at each wind direction cause the domain height L_z and vertical number of cells N_z to be slightly different: 1.172 km and 84 cells for case 100°, 1.305 km and 86 cells for 240° and 1.267 km with 85 cells for 290°. Thus, mesh sizes, in millions of cells, are ≈ 40.85 (100°), ≈ 41.81 (240°) and ≈ 41.33 (290°). The mesh is created employing CENER-WindMesh (Gancarski and Chávez-Arroyo, 2017; Ivanell et al., 2018). The adequacy of the grid resolution is discussed in the Results section.

The ASL-derived forest density map is used to create the PAD field within the farm and transition zones by linearly interpolating between the 10 m × 10 m input fields and the mesh. In the buffer, a uniform value of PAD = 2.813 1/m is set within a constant tree height of 14.38 m, corresponding to the average height of the forest in the input map. The ground surface is

https://doi.org/10.5194/wes-2025-114
Preprint. Discussion started: 14 July 2025

set as a wall with a uniform roughness of $z_0 = 0.03$. All the lateral boundaries are set to periodic, so the flow is recycled as it leaves the outlet and the sides. Simulations are run under neutral conditions, with the top boundary set as a symmetry plane. The flow itself is driven by a constant and vertically uniform pressure gradient that is calculated on the basis of the geostrophic velocity vector $\boldsymbol{u}_g$ (see Bautista, 2015), in addition to a Coriolis forcing corresponding to a latitude of 57°. To find the right magnitude and direction of $\boldsymbol{u}_g$ for each case, a calibration procedure was devised, with the goal of approximating the desired target velocity of $|\overline{\boldsymbol{u}}| = 7.4$ m/s and the given wind direction φ at $z_{\text{agl}} = 100$ m (height above ground level) at the at the metmast location. It starts by finding $\boldsymbol{u}_g$ that yields the desired target velocity in preceding run over a domain with the same dimensions and numerical parameters but with a coarser mesh of 50×50 m horizontal resolution within the farm region. That $\boldsymbol{u}_g$ vector is then used to drive the simulations (above described mesh), with an initial velocity field of zero. Subsequent adjustments to $\boldsymbol{u}_g$ were made up until 240×10^3 s and from then on, simulations were run with a fixed $\boldsymbol{u}_g$ for a total of 400×10^3 s. The convergence of the flow solution was verified to have been fulfilled by observing that profiles of $\overline{u_i'^2}$ calculated in successive periods of 20×10^3 s had reached a quiescent state. Velocity time series and other data employed for the results are extracted during a subsequent sampling period of 20×10^3 s to the initial run at every cell centre on a vertical column at the metmast location. For this, a fixed time step of $\Delta t = 0.296$ s was used, corresponding to a maximum Courant-Friedrichs-Lewy number over all the domain of CFL ≈ 0.6. The geostrophic wind vector derived from the calibration procedure as well as the averaged velocities obtained during the sampling period are shown in Table 1.

Table 1. Mean velocities and directions at $z_{\text{agl}} = 100$ m and the geostrophic wind employed in driving the flow for the Ryningsnäs cases.

Case	u_s at 100 m [m/s]	φ at 100 m	$\lvert\boldsymbol{u_g}\rvert$ [m/s]	φ_g
100°	7.71	100.80°	11.5	123°
240°	7.05	242.11°	12.5	263°
290°	7.72	291.67°	11.4	312°

4.2.3 Numerical setup 3: assessment of terrain and forest conditions on footprint

An additional set of simulations is carried out with the objective of evaluating the effect that the representation of the terrain and forest features have on the prediction of the wind characteristics at a given location. Based on the domain layout employed in Sec. 4.2.2 for the incoming direction of 240° (identified as R3.0), three additional setups labelled R3.1 to R3.2 with the exact same dimensions are created but with the following distinctive configurations:

R3.1 A domain where the ALS-obtained PAD distribution, i.e. the *realistic forest*, is constrained to a smaller area around the metmast of 3 km + 2 km (upstream + downstream) in length and 5 km in width. Outside this region, the forest density is uniformly set to the approximate average value of the forest density upstream the metmast for the 240° direction, $\text{PAD} = 0.12\ 1/\text{m}$, with a height equal to 14.38 m (the mean of the forest map).

https://doi.org/10.5194/wes-2025-114
Preprint. Discussion started: 14 July 2025

R3.2 A domain with a *flattened* ground, with a constant elevation set to 122.67 m above sea level, equal to the terrain elevation at the location of the metmast. Forest distribution is the same as in the reference 240° configuration R3.0.

R3.3 A domain with a uniform forest distribution, $\mathrm{PAD} = 0.12\ 1/\mathrm{m}$ with a constant height of 14.38 m. The terrain elevation is the same as in the reference 240° configuration R3.0.

In cases R3.1 and R3.3 the mesh is the same as in the 240° reference case, while for the case R3.2 a slight variation in the vertical direction occurs due to the flattening of the elevation differences at the ground. The latter has $N_z = 85$ cells with the first node at $z_1 = 1.778$ m, in comparison to the values of the reference 240° case of $N_z = 88$ cells and $z_1 = 1.727$ m. Cases R3.1 and R3.3 have one caveat: a fully uniform tree height would require a uniform layer of cells at the canopy top that is not possible to obtain for such a short height above a terrain with the complexity of the chosen site. However, as the mesh is the same as the one used in the reference 240° case set with a realistic PAD distribution, the comparison with that case is made over terrains representing the same complexity and its ensuing effects on the wind above. In cases R3.1 to R3.3 the flow is driven by the same parameters as in the 240° case (Table 1) with the same boundary conditions. Simulations are run during 240×10^3 s to attain flow convergence and then, as in the 240° reference case, an additional 20×10^3 s period with $\Delta t = 0.296$ s to record velocity time series and other data at every cell centre along a vertical column at the metmast location.

5 Post processing

This section describes the post processing and unless explicitly stated, this was performed in the same way for the measurements and the simulations. For the measurements, the time series was split into 30 minute long periods with a sampling rate of 20 Hz. In order to retrieve comparable data from the simulations the time series sampled from the vertical array described in Sec. 4.2.1 were used. At each height the reference frame was rotated according to the direction of the local mean wind in the same way as described in Sec. 3.2. Fluctuating variables where also constructed in the same way, with the difference that the whole 20000 s period was regarded as the averaging period. Tests were made also splitting the LES simulations in 30 minute blocks, which did not visibly impact the results, apart from the obvious effect of filtering out low frequencies in the spectra.

Statistical processing for the measured turbulence was the same as in Arnqvist et al. (2015), with the most important steps repeated below for convenience. The 20 Hz data was split into 30 minute bins, after which fluctuations where constructed by removing the arithmetic mean. The data was rotated locally (i.e. at each height and 30 minute period) into the direction of the horizontal mean wind, with u, v and w describing the streamwise, spanwise and vertical wind respectively. Higher order moments were constructed by multiplication of fluctuation velocities, for example the streamwise shear stress:

$\overline{u'w'}$,

where $u' = u - \overline{u}$ and $w' = w - \overline{w}$ are the fluctuating streamwise and vertical velocities and the overbar denotes temporal average.

https://doi.org/10.5194/wes-2025-114
Preprint. Discussion started: 14 July 2025

5.1 Spectral statistics

Spectral statistics were calculated by a Fast Fourier Transform (FFT). A cross-spectral tensor, $\phi(u_i, z_k, u_j, z_l)$ was created for all possible separations along the metmast ($z_k \in [40,\ 59,\ 80,\ 98,\ 120,\ 138]$ m height) and variable combinations ($u_i \in [u,\ v,\ w]$) by taking the outer product of all velocity components transform signals (FFT of u', w' or v' at all measurement heights) with their complex conjugates. The spectral tensor as well as the frequency vector was then averaged in 20 logarithmically spaced frequency bins for each 30 minute time series. To examine how realistic the LES turbulence would appear for a hypothetical wind turbine rotor, some specific cross-spectral measures were used.

Single point power spectra and cospectra, $\Re\phi(u_i, z_k, u_j, z_k)$ was used to evaluate the impact of the filter scale on the character of single point turbulence. The spectral density was pre-multiplied with the frequency and normalized by the total turbulence kinetic energy. The frequency was normalized by multiplication with z_k/U_k.

To evaluate the effect of turbulence on larger sections of the rotor, the two-point cross-spectra, $\Re\phi_{u_i,z_k,u_i,z_l}$ and the coherence

$$\mathrm{Coh}(u_i, z_k, u_i, z_l) = \frac{|\phi(u_i, z_j, u_i, z_k)|^2}{\phi(u_i, z_k, u_i, z_k)\phi(u_i, z_l, u_i, z_l)}, \tag{17}$$

was examined.

To determine the slope of the eddies, the phase lag in radiance was examined between between two different heights z_j and z_k,

$$\Delta\theta(u_i, z_j, u_i, z_k) = \arctan\left(\frac{\Im\phi(u_i, z_k, u_i, z_l)}{\Re\phi(u_i, z_j, u_i, z_k)}\right), \tag{18}$$

was used.

For the statistics processing of LES from Sec. 4.2.1, sampling probes are located at each cell centre over the 9 columns layout as in Fig. 1. Spectra, integral time scales and high order statistical quantities are presented as horizontal plane averages, i.e. the average of all 9 values at the same height. In the case coherences, the average is made over 9 location pairs. The supplementary logarithmic average applied to spectra is referred to as smoothing as well.

5.2 Integral time scales

Integral time scales were calculated for both the simulations and the measurements by taking the FFT of the spectral density and dividing with the variance to find the auto-correlation function (Wyngaard, 2010, eq. (15.14)). The value of the integral time scale, $\mathcal{T}$, was then estimated by finding the time lag for which the auto-correlation fell below $\exp(-1)$, in accordance with Kaimal and Finnigan (1994). Other methods to find $\mathcal{T}$ were also tested and gave similar results. The lengthscales are obtained simply by multiplying with the mean velocity at each location.

https://doi.org/10.5194/wes-2025-114
Preprint. Discussion started: 14 July 2025

5.3 Confidence levels

5.3.1 Measurements

Confidence levels around the long term mean values were estimated by the standard error of the 30 minute averages. 95 % levels were estimated as 1.96 of the standard error, assuming that each 30 minute mean is statistically independent from the others and that the 30 minute means are normally distributed around the long term mean.

5.3.2 LES

When comparing with measurements, confidence levels are also calculated for LES (sections 6.2 and 6.3). Since the mean values for the LES data were constructed from a single time series, the confidence levels were determined in a different way from the measurements. For the mean wind, the relative random error variance, e_u of the time series was estimated, following Lumley and Panofsky (1964), by

$$e_u = \frac{2\mathcal{T}_1 \overline{u'^2}}{T\overline{u}^2}, \tag{19}$$

where T is the length of the time series and $\mathcal{T}_1$ is the integral time scale of u. For the second and third order moments the formulation from Lenschow et al. (1994) was used

$$e_{\overline{u_i u_j}} = \frac{2\mathcal{T}_{ij}}{T}, \tag{20}$$

where $\mathcal{T}_{ij}$, the integral time scale for the covariance, was estimated as $\mathcal{T}_{ij} \approx \sqrt{\mathcal{T}_i \mathcal{T}_j}$. Only the isotropic third order moments were evaluated, and here we also follow Lenschow et al. (1994):

$$e_{\overline{u_i^3}} \approx \frac{6\mathcal{T}_i}{T}. \tag{21}$$

The first and second order velocity moments have been normalized by the kinetic energy at the scaling height, so to derive appropriate confidence intervals the relative random errors were first raised to the exponent $1/2$, then multiplied with the dimensional quantity of interest and normalized again by the scaling factor. Finally, it was assumed that the uncertainty follows a Gaussian distribution so that 95 % confidence levels could be obtained by multiplication with 1.96. To give an example, the confidence interval of the horizontal variance was calculated by $(2\mathcal{T}_{11}/T)^{1/2}\overline{u'u'}/k_{sc}$. It should be noted that this procedure omits the random error due to the statistical uncertainty of the scaling factor, which was neglected due to difficulties in estimating its correlation with the random error of the investigated variable itself. Since most scaled variables are $\mathcal{O}(1)$ this added uncertainty could be expected to contribute to a widening of the confidence intervals by a factor between $\sqrt{2}$ and 2 depending on the correlation between the random errors (assuming standard error propagation rules for division and equal sizes of the relative random error). Given the already approximate nature of the confidence interval estimation this was not added, and the confidence intervals should only be considered as an indication of the statistical uncertainty.

https://doi.org/10.5194/wes-2025-114
Preprint. Discussion started: 14 July 2025

6 Results

6.1 Wall model and forest implementation and study

The first part of the results section comprises the simulation of the wind flow over ideal conditions of terrain and forest coverage to observe the performance of the numerical model and see its validity. Specifically, a set of variations in the SGS model, PAD and z_0 are chosen to contrast some of the turbulence features yielded in each case. The cases are listed on Table 2. These can be grouped in 3 categories according to the verification purpose:

1. To compare the results produced by the forest model with those produced by a wall model that only employs z_0.

2. To assess whether there is impact on the wind flow produced by varying the ground roughness in a simulation that also employs PAD-based drag.

3. To examine the effect of varying the tree density within the forest. This comprises the observation of the significance of including an enhanced subgrid dissipation term for the forest — $\varepsilon_{\text{SGS},f}$ in eq. (13) —.

Table 2. Simulation cases for model verification. Cases F1 to F8 employ an explicit model of the forest while F8 and F9 only use a wall model without a forest representation.

Case	PAD	z_0	SGS	Enhanced ε_{SGS}	Remarks
F1	0.15	0.03	Y. $k-$eq.	yes	Reference case
F2	0.15	0.5	Y. $k-$eq.	yes	Forest with high roughness
F3	0.15	No WM	Y. $k-$eq.	yes	Only forest
F4	0.15	No WM	Y. $k-$eq.	no	No enhanced dissipation
F5	0.15	No WM	Smag.	no	Change of SGS model
F6	0.018	0.03	Y. $k-$eq.	yes	Forest with low PAD
F7	0.018	0.5	Y. $k-$eq.	yes	Forest low PAD and high roughness
F8	No Forest	0.03	Y. $k-$eq.	no	Wall model only
F9	No Forest	0.65	Y. $k-$eq.	no	Wall model only, forest-equiv. roughness

The simulations are run based on the numerical setup described in Sec.4.2.1, employing a flat ground surface with —for the applicable cases— a uniform roughness and/or a forest of uniform tree height of $h_f = 20$ m. In most cases with forest, PAI $= 3$ is used yielding a tree density of PAD $= 0.15$ 1/m. This is the value employed in the reference case F1. In two other cases (F6, F7) PAI $= 0.36$ corresponding to PAD $= 0.018$ 1/m which is used as the value for the low density cases. The roughness length in case F9 is calculated as the equivalent for a forest with PAI$= 3$ and a height of 20 m (Mohr et al. (2018), equation 9-16 and 9-17) which yields $z_0 = 0.65$ and a displacement height of $d = 17.01$ m. Results from this case, also referred to as PAD-equivalent, are shown with an upward shift i.e. $z + d$.

https://doi.org/10.5194/wes-2025-114
Preprint. Discussion started: 14 July 2025

6.1.1 Impact of modelling parameters on flow characteristics

Fig. 3 compares the results of the profiles of the velocity magnitude and wind direction between the forested cases (F1, F7) and setups without and explicit forest representation (i.e. without a PAD field) but with a rough surface at the bottom, simulated by means of a wall model. For the latter, two roughness values have been chosen, the $z_0 = 0.03$ m used for the reference model (case F8) and a value that has been derived as the PAD-equivalent $z_0 = 0.65$ m (F9). The case F7 is also included to observe the influence of a high roughness in a forest with low density. The results in Fig. 3 (a)-(b) for the horizontal mean velocity magnitude u_s (used henceforward without a bar) show that the drag effect is the largest everywhere for the reference case F1 and the smallest for F8, as expected. The PAD-equivalent roughness in F9 produces noticeably different results than the reference case, even when considering the displacement height, a match is seen until at about 850 m. The usage of low PAD and high z_0 in F7 results in a velocity profile with a slope opposite to F1 and values of u_s in between those of F1 and F9, showing evidence of the effect of the high roughness within the low density forest. The same z_0 is not seen to produce the same result with a higher PAD (case F2), as seen below. Fig. 3 (c) displays a comparison of the turning of the wind within the forest, where $\varphi = 270$ deg corresponds to a flow moving in the longitudinal direction, aligned with the $x-$axis of the domain. The turning is seen to be the largest for F1, with the low PAD and wall-model-only cases showing much less deviation in comparison. Notably, the low PAD case F7 displays a minimal turning but a distinct wind direction that denotes the influence of the drag of the forest, despite its low density, in setting the wind direction above it. Also, it is worth noting that the wind direction above the forest cannot be reproduced by the PAD-equivalent roughness simulation. Fig. 3 (d) compares the total TKE, highlighting the differences produced within the forest due to the PAD variation or its absence. In spite of this, F7 quickly reaches the same level as F1 above the canopy, due to the higher flow velocity. Meanwhile, the non-forested cases F8 and F9 show a significantly lower level in comparison.

Fig. 4 compares the velocities, vertical wind shear du_s/dz, resolved TKE k_{res} and its ratio with respect to the total amount $k_{\mathrm{tot}} = k_{\mathrm{res}} + k_{\mathrm{SGS}}$ between the reference forest model (F1) and forest models with higher roughness (F2) and lower PAD (F6 and F7). The reduced forest drag of the latter leads to an acceleration of the wind profiles, as expected. Inside the canopy, the velocity profiles of the low-PAD cases F6 and F7 can be regarded as an intermediate point between the u_s curves of a wall-model only (F8 in Fig. 3 (b)) and the reference PAD case F1, where the region near the top of the forest layer drives a change in the concavity of u_s. This can be recognized as a feature of the transition between a boundary layer and the mixing-layer that arises when forest density increases (Raupach et al., 1996). A key aspect of the mixing layer analogy for forest flows is the inflection point in the velocity profile near the canopy top, clearly seen in F1 as well as other cases with the same PAD. In Fig. 4 it can also be seen that despite the increased z_0 in F2 from that of F1, the PAD value seems large enough as to control the flow characteristics and produce nearly identical results within the forest and above, except for the first couple of cells above the ground where k_{SGS} for F2 is slightly larger, shown indirectly via $k_{\mathrm{res}}/k_{\mathrm{tot}}$. Conversely, PAD in cases F6 and F7 is lower and the different values of z_0 produce discernible variations within the forest, specially in vertical shear, but only in the case of u_s the difference is maintained also above the forest. Furthermore, while in the cases F1 and F2 the near ground fluctuations are mostly resolved by the LES, the lower PAD in F6 and F7 causes a noticeable increment on the SGS component, observed as a

https://doi.org/10.5194/wes-2025-114
Preprint. Discussion started: 14 July 2025

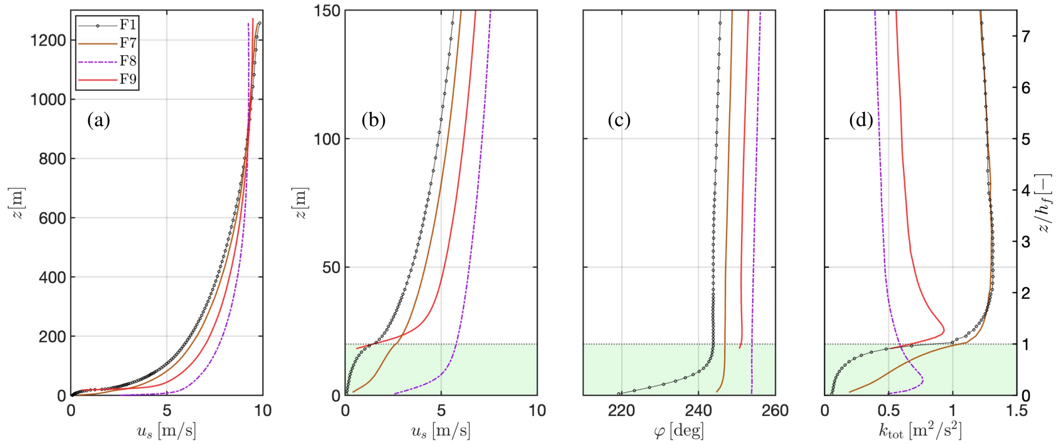

Figure 3. Comparison of the horizontal velocity magnitude over the entire domain height (a) and the first 150 m (b), wind direction (c) and total TKE (d) between cases with an explicit forest modelling (F1, F7) and those with only a wall model (F8, F9). The vertical region covered by the forest is displayed as a green shaded area.

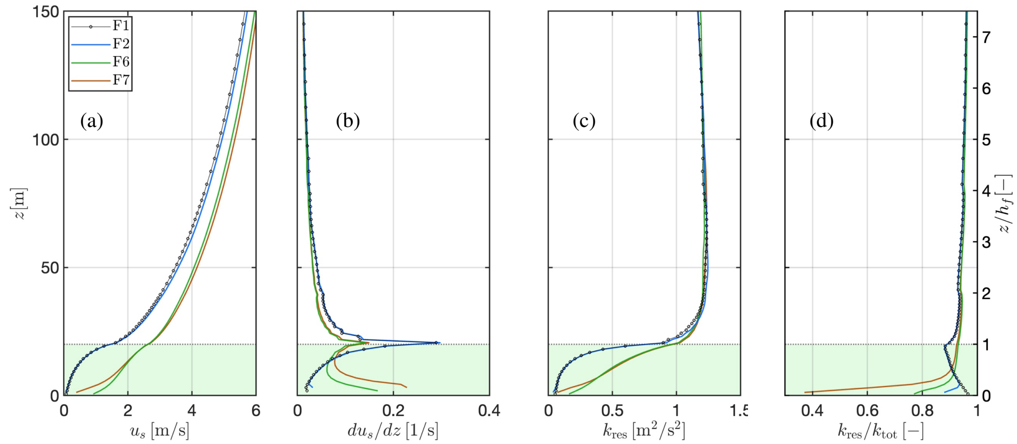

Figure 4. Variation of modelling parameters in cases with explicit forest model. From left to right: velocity (a), vertical wind shear (b), resolved TKE (c) and resolved to total TKE ratio (d).

strong reduction of $k_{\mathrm{res}}/k_{\mathrm{tot}}$ as shown in Fig. 4 (d). Note that in this figure it is possible to see the transition between the mesh refinement zones at $z = 40$ m and 80 m (see Sec. 4.2.1) but this has no effect on the results and their analysis.

The next comparison focuses on the impact of the modelling choice for the subgrid component within and above the forest. Fig. 5 shows vertical profiles of u_s, k_{res}, k_{SGS} and the ratio resolved to subgrid $k_{\mathrm{res}}/k_{\mathrm{tot}}$ for cases F1 to F5, all of which use the same PAD value. In spite all variations in near-wall treatment, the velocity profiles yielded by all these setups are essentially identical. Also, it can be seen that k_{res} is nearly equal above the forest except for a minor increase from the Smagorinsky SGS

https://doi.org/10.5194/wes-2025-114
Preprint. Discussion started: 14 July 2025

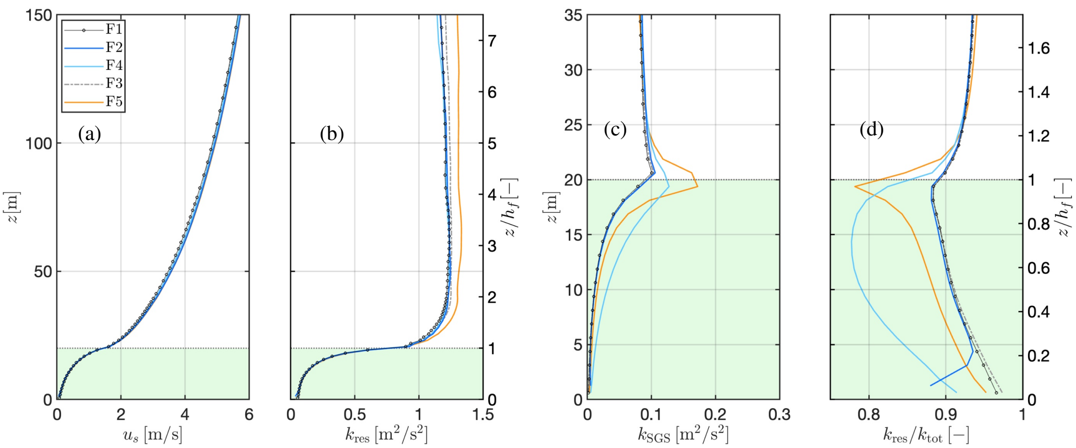

Figure 5. Variation of turbulence modelling values. From left to right: velocity (a) and resolved (b), subgrid (c) and resolved-to-total ratio (d) of TKE for the forested cases.

model in F5. More differences can be appreciated in $k_{\rm SGS}$. For that, the absence of the extra dissipation term eq. (15) in F4 shows an ensuing increase in the subgrid turbulence component, which can be also observed as a reduction —with a minimum just below the forest edge— in the profile of $k_{\rm res}/k_{\rm tot}$. This occurs only within the forest, the only region affected by the dissipative term $\varepsilon_{{\rm SGS},f}$ of eq. (15). The usage of Smagorinsky, which also lacks $\varepsilon_{{\rm SGS},f}$, is shown to produce a greater increase of $k_{\rm SGS}$ but only around the forest edge. Make note that Smagorinsky is employed without a wall model which permits to analyze its performance within the forest separately from that near the ground.

The results of F5 show a reduction of the resolved portion of the turbulence, peaking at the forest edge as well. It can also be seen that using Smagorinsky leads to a slight increase in $k_{\rm res}$ above the forest that persists along the ABL height (here shown only for the first 150 m). This result is consistent with the observations of overdissipation yielded by this model near the ground, but since no rough surface is used, such effect is then emphasized from the forest edge and above. It has been argued that the overdissipation can lead to an overestimation of the mean velocity in lower parts of the ABL (Porté-Agel et al., 2000; Pope, 2000). However, neither Smagorinsky nor other of the modelling variations (F1 to F5) are observed here to affect the velocity profile noticeably, neither within or above the forest. Furthermore, except for the Smagorinsky model, the level of total turbulence kinetic energy does not appreciably change between the different modelling choices.

6.1.2 Spectral analysis

The next part of the study focuses on the turbulence characteristics of 3 simulation cases: the reference case F1 as well as F6 and F9. This permits to contrast the results of simulations that explicitly consider forest —with two different densities— with one that employs instead a PAD-equivalent ground roughness. The one-point spectral properties are examined first, these are calculated from the full time-series of the LES (see Sec. 4.2.1) at different heights following the methods described in

Sec. 5.1. To facilitate the visualization, each curve is smoothed by applying a further averaging using 25 bins logarithmically distributed. It is possible to observe the effect of the smoothing procedure as the non-smoothed spectra of the reference case is also shown in each figure. Spectra are shown at heights of 25, 100 and 200 m, to represent the near forest as well as typical turbine positions. Displacement height is considered for the case F9, subtracting the value of d to these positions.

The auto-spectra of the longitudinal fluctuations are shown in Fig. 6. The results show the development of the characteristic slope of the subinertial range, visible at the heights 100 m and 200 m for all cases. Whereas the power spectrum of the low PAD remains very similar to the reference case for all heights, case F9 displays a noticeable lower level of energy for most of the scales except for the lowest height, an outcome consistent with the comparison of k_{tot} in Fig. 3. While this supports the ability of the wall-model –with consideration of the displacement height– to represent the energy distribution of longitudinal velocities for lower regions, it underestimates it for regions covered by a wind turbine rotor.

Fig. 7 shows the frequency-premultiplied cospectra of uu, vv, ww as well as the cross-components uw at different heights. This permits to observe the proportions in energy content between the different components for each setup, as well as their energy distribution as function of frequency. As expected, longitudinal fluctuations observe the largest levels of energy, followed by the lateral, vertical and the cross-component uw. A redistribution of energy towards smaller frequencies is observed when the height increases, with the spectra maxima moving towards the left. This can be seen in all components except for ww, in part due to the difficulty to resolve the small vertical fluctuation scales (considerably smaller than those in the horizontal components) at this level of mesh refinement. Instead, the energy of the ww spectra becomes somewhat more distributed (or flattened) along the frequencies. The spectral energy of ww and uw of the case F9 is close to zero for the lowest elevation, due to its proximity to the ground that limits the size of the eddies. Yet, their values at 100 m and 200 m remain distinctly lower compared to F1 and F6. Something similar occurs with the energy of the lateral fluctuations vv which is persistently smaller for F9 than for the other cases. Furthermore, a strong decay in energy in longitudinal velocities seen for the case F9 from the 25 m height in Fig. 6 (a) in comparison with (b) 100 m and (c) 200 m. These differences reveal contrasting characteristics in the representation of turbulence when representing forest drag compared to an approach based exclusively on a wall-model. Notably, the lower energy levels in uw reflect a limited strength in momentum flux. Conversely, the spectral curves of F1 and F6 show similar values in all components despite the differences in leaf density. Two key distinctions can be discerned, firstly, it is found in ww at the 25 m height, where the maximum energy of F6 is somewhat greater and also position at higher frequencies. This arises from the larger permeability to vertical velocities due to the lower PAD. The second distinction concerns the intensity and position of peaks. Indeed, horizontal components show prominent peaks at frequencies $\sim 6\times10^{-4}$ 1/s and $\sim 2\times10^{-3}$ 1/s that can be associated to the dimensions of the domain. The first one corresponds to a time event of about 1667 s, linked to the recycling period of the flow in the domain, covering a distance slightly larger than L_x according to the wind directions shown in Fig. 3. This peak is more prominent for F6, pointing to a stronger effect of the recirculation for lower forest densities. The second peak occurs for events of approximately 500 s, which would correspond to the eddy turnover time $\sim H/U$. Therefore, this peak signals the scale of the largest structures in the simulation, indicating the location from where the energy decays towards smaller values at larger frequencies.

https://doi.org/10.5194/wes-2025-114
Preprint. Discussion started: 14 July 2025

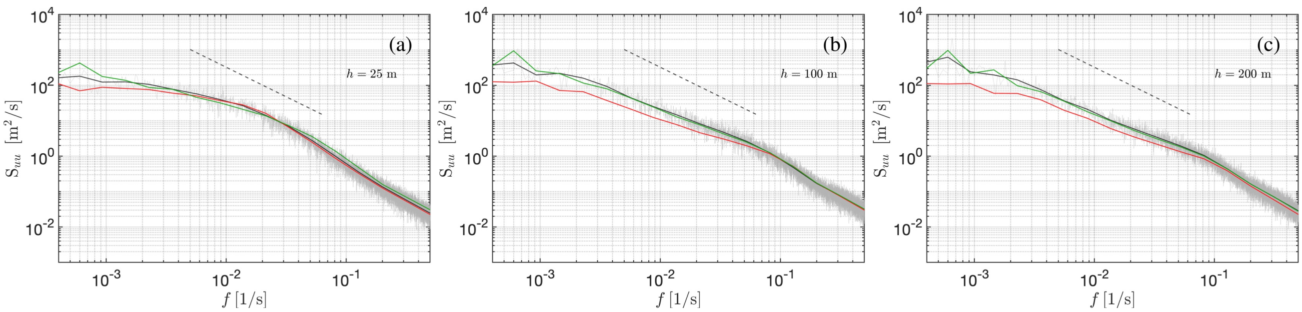

Figure 6. Power spectral density of the longitudinal velocity at $z \approx 25$ m (a), 100 m (b) and 200 m (c). The pre-smoothed spectra of F1 is shown as a grey line. The dashed line corresponds to the -5/3 slope.

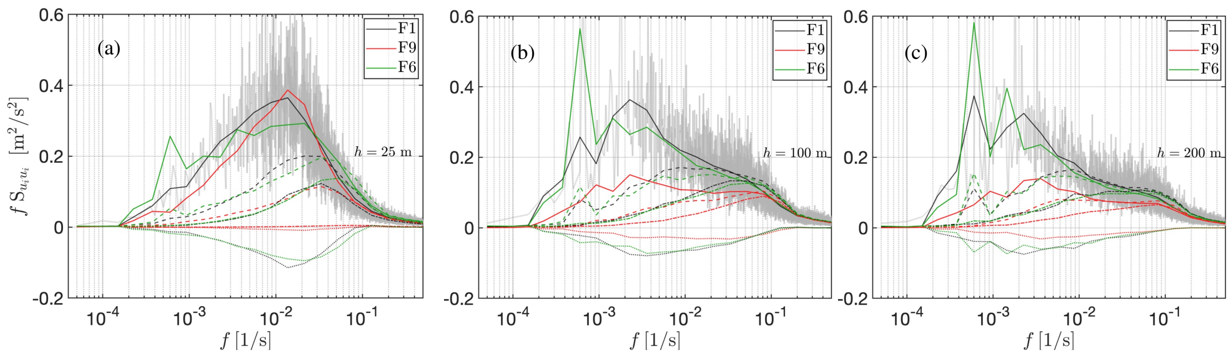

Figure 7. Comparison of premultiplied power spectral density of uu (solid lines), vv (dashed), ww (dot-dashed) and cross-spectral density uw (dotted) fluctuations the heights of 25 m (a), 100 m (b) and 200 m (c). The pre-smoothed uu spectra of F1 is shown as a grey line.

The calculation of coherence permits to quantify the maximum correlation of the velocity component at a given turbulence scale. Spectral coherences are calculated for the cases F1, F6 and F9 for three different vertical separations $\delta_z = 20$, 40 and 80 m, set within the hypothetical rotor area. This is done using eq. (17), based on the calculation of the two-point cospectrum and one-point spectrum of the two locations. As pointed out by Kristensen and Jensen (1979), it is required that the calculation of spectra includes a procedure resembling an ensemble average, in this case block average, to avoid that the resulting coherence takes a value of unity for all frequencies. Therefore, the time-series at each sampling point is divided in blocks of about 1 h duration with 50% overlapping, from which individual spectra are obtained and later averaged. The process is repeated for each of the 9 locations of equal height, whose average yields a single spectrum. Finally, this spectrum is logarithmically smoothed with the procedure described earlier. All spectra used in eq. (17) are obtained in this way, yielding the coherences shown in figures 8 to 10. To observe the effect of smoothing in the calculations, the figures also include the coherence obtained with spectra that have not been smoothed, but only for the case F1. The coherences of longitudinal velocities obtained with the model of Davenport (1961) included in the standard by IEC (2019) are shown for comparison.

https://doi.org/10.5194/wes-2025-114
Preprint. Discussion started: 14 July 2025

For the first separation of 20 m, between $h_1 = 80$ m and $h_2 = 100$ m, the energy distribution showed by the coherence of the longitudinal velocity component is shown in Fig. 8 (a). There, differences are rather minimal between the outcomes of the three different setups while comparing well to the IEC prediction except for the highest decade of normalized frequencies. Figures 8 (b) and (c) compare results for the lateral and vertical velocity components, respectively, showing a large correspondence between coherences of F1 and F6 while F9 are slightly below. For the 40 m separation, longitudinal coherences in Fig. 9 (a) are again very close among the different setups. These curves show a small drop in correlation compared to the 20 m separation but also a lower value than the projection of IEC that now extends over a large part the frequency range. In Fig. 9 (b) the distinct maxima of coherence of setups F1 and F9 reveal that turbulence structures have a characteristic lateral extension, shorter compared to F6. Fig. 9 (c) shows a noticeable drop in the maximum coherence of the vertical motions, seemingly due to a structural tilt in turbulence as well as phase changes with height, which become more evident with increasing separation. The drop occurs for the three cases although case F9 stands out due to its greater value around the smallest frequencies. The same trends are observed for the largest separation of 80 m. Fig. 10 (a) shows a small reduction in longitudinal correlation, with the values remaining consistent among all cases as well as largely below the value predicted by the IEC curve Fig. 10 (b) displays that correlation maxima related to the limited lateral extension of the turbulence structures, with F6 being the largest (as in the previous case $\delta_z = 40$ m) but now F9 exhibiting a more pronounced drop than case F1. Fig. 10 (c) shows that correlations of vertical velocities continue decreasing, with F9 showing the highest values.

In general, results shown in figures 8, 9 and 10 display a strong coherence for the longitudinal velocity component along the frequency range for all cases, that is largely maintained for the three separations. Conversely, lateral and vertical components show a strong correlation only for the smallest separation of $\delta_z = 20$ m. For $\delta_z = 40$ m and 80 m, the shape of coherences of the lateral component suggest that the turbulence structures have a characteristic width, largest for F6 and shortest for F9. Meanwhile, the coherence of the vertical velocity decreases more markedly with increasing separation but less so for case F9. On one hand, this reflects the need of a larger mesh refinement to reproduce the comparatively smaller velocity fluctuations in this direction. But more significantly, the larger values displayed by F9 give an indication that the greater shear in the forested cases produces a stronger distortion in the eddies, reducing their coherence in that direction. This supports what was already determined from the spectral results in Fig. 7: cases with an explicit forest modelling can not only change the energy level of vertical fluctuations but also its distribution, a feature that is not replicated by a roughness-based modelling. For the lateral correlations a more significant drop is noted, pointing to an underestimation of the width of the eddies by the wall model F9, which accompanies the greater one-point spectral density of the lateral velocities observed in Fig. 7 from the forest models in comparison to F9.

Lastly, the smaller coherence values consistently displayed in the longitudinal direction with respect to the IEC standard represents an interesting outcome. Coherences obtained from experimental results also show correlations below the IEC prediction, for different separations (Sec. 6.2). In all these cases, results are displayed with a normalization for the frequency axis where $\overline{u}_{h_1,h_2}$ represents the mean of the average velocities at each point. The IEC model presents this velocity as the one measured at the hub, so in the absence of a wind turbine some ambiguity appears when the model is applied to estimate coherence over any set of positions. Here we use $\overline{u}_{h_1,h_2}$, that albeit a natural choice, might not represent the most suitable for the IEC

https://doi.org/10.5194/wes-2025-114
Preprint. Discussion started: 14 July 2025

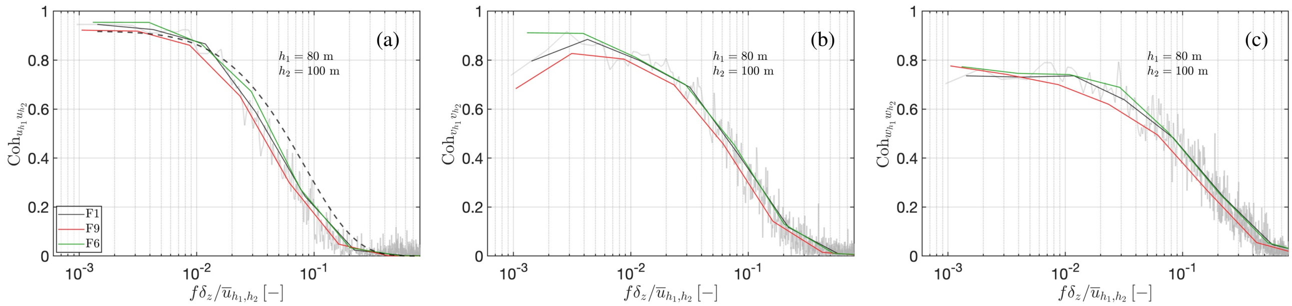

Figure 8. Coherences of longitudinal (a), lateral (b) and vertical (c) fluctuations for a vertical separation of $\delta_z \approx 20$ m. The coherence from the pre-smoothed of F1 is shown as a grey line. The dashed line in (a) corresponds to the coherence model of the IEC (2019).

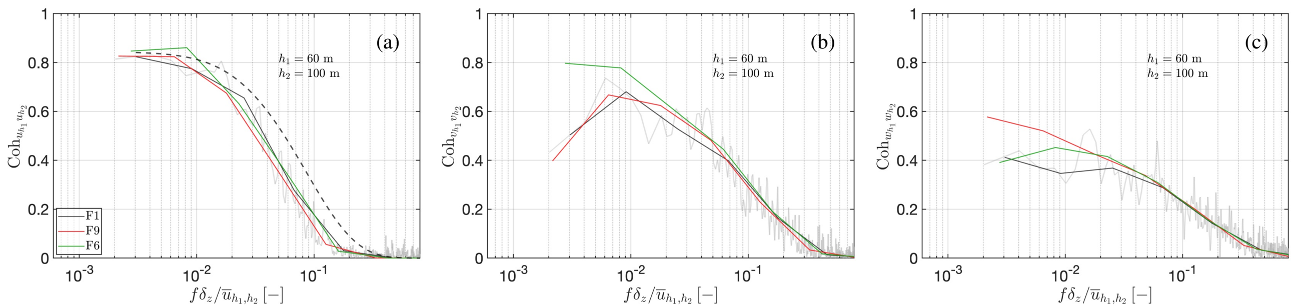

Figure 9. Coherences of longitudinal (a), lateral (b) and vertical (c) fluctuations for a vertical separation of $\delta_z \approx 40$ m. The coherence from the pre-smoothed of F1 is shown as a grey line. The dashed line in (a) corresponds to the coherence model of the IEC (2019).

model. Indeed, the IEC curve would provide a better match to the LES results if shifted towards smaller frequencies, something that can be quickly achieved by using smaller values of velocity than $\overline{u}_{h_1,h_2}$. A limited evaluation shows that reducing the velocities by about 30% made for a better comparison of the IEC standard, although better predictions could be obtained with adjustments depending on both the separation and height of the positions in question. Therefore, the discrepancy can be explained rather as a question of normalization instead of being related to a more fundamental issue.

6.1.3 Integral lengthscales and high order moments

Fig. 11 shows the integral lengthscales in the longitudinal, lateral and vertical directions obtained from the autocorrelation of ~ 1 h blocks of the velocity time-series as described in Sec. 5.2. The region of uniform PAD employed in F1 and F6 is shown as a green shade. Note that the results for F9 are elevated by d. Differences between the modelling setups appear from within the forest canopy and extend towards the wind above. Inside the canopy, the low forest density case F6 exhibits larger lengthscales compared to F1. Above it, growth rates are somewhat different among the three setups but their trends remain comparable in all directions. F6 shows the fastest growth while F9 presents the slowest, resulting in larger lengthscales for F6

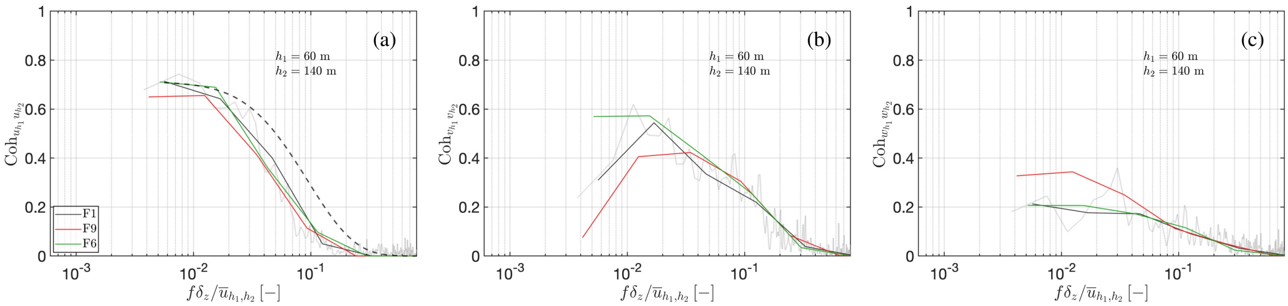

Figure 10. Coherences of longitudinal (a), lateral (b) and vertical (c) fluctuations for a vertical separation of $\delta_z \approx 80$ m. The coherence from the pre-smoothed spectra of F1 is shown as a grey line. The dashed line in (a) corresponds to the coherence model of the IEC (2019).

above the canopy in all directions. It can be observed that F9 underestimates the lenghscale produced by the reference case F1 in all directions, except the region below $\sim 5h_f$ for L_{uu}. The magnitudes of lengthscales are noticeably different in each direction although it can be appreciated that proportions are maintained, namely $L_{uu} \sim [3L_{vv}, 4L_{vv}]$ and $L_{vv} \sim [3L_{ww}, 4L_{ww}]$ (note that the maximum value shown in x-axis in each subfigure of Fig. 11 follows $9L_{ww} = 3L_{vv} = L_{uu}$).

The values of the lengthscales at the canopy top are, for L_{uu}/h_f, ≈ 1 (F1, F9), ≈ 3.75 (F6); for L_{vv}/h_f, ≈ 1.25 (F1, F9), ≈ 1.25 (F6) and for L_{ww}/h_f, ≈ 0.5 (F1, F9), ≈ 0.75 (F6) and ≈ 0.85 (F9). Raupach et al. (1996) shows that for a large variety of field and wind-tunnel data, $L_{uu}/h_f \sim 1$ and $L_{ww}/h_f \sim 1/3$, which is roughly fulfilled by the reference case. A reduction in L_{uu} and L_{ww} with PAD within and above the canopy is expected, as demonstrated in studies compiling several measurement results (Raupach et al., 1996; Brunet, 2020). The same trend is observed when comparing F1 and F6 in the results of Fig. 11 (a) and to a lesser extent in (c). It is worth noting that Brunet (2020) emphasizes that lengthscales obtained from one-point statistics as applied here might be underestimated inside the canopy, since the values obtained from two-point statistics in this region are generally smaller. This is due to the fact that unlike the latter, the former method derives the lengthscales in function of the mean wind, but the convection velocity of turbulence eddies around the canopy height is seemingly twice that of u_s. This mean velocity u_s is used as a characteristics velocity to convert the integral time scale $\mathcal{T}$ to length but alternatives exist, such as using $\sqrt{k_{\text{res}}}$ or $\sqrt{k_{\text{tot}}}$ in a similar way to Katul and Chang (1999).

Higher order moments are also calculated for F1, F9 and F6. Fig. 12 shows the skewness inside and above the canopy for the three components of the velocity fluctuations. While the lateral component remains close to zero throughout, the longitudinal and vertical skewness, Sk_u and Sk_w respectively, show a noticeable asymmetry in their distributions within and above the forest. The positive values of Sk_u are indicative of strong turbulence in the form of gusts on the slow moving flow, while the negative values in Sk_w signify that downwards motions are greater in magnitude than upwards. This is consistent with skewness observations made from various vegetation canopies accompanied by quadrant analyses by Raupach et al. (1996) and Brunet (2020), revealing an infrequent but strong penetration of high speed wind moving downwards into the canopy. Sk_u of F6 remains mostly larger throughout the canopy which combined with a slightly larger magnitude of Sk_w, suggests stronger downwards sweeps of turbulence compared to F1, likely due to the reduced forest density. The results display changes with

https://doi.org/10.5194/wes-2025-114
Preprint. Discussion started: 14 July 2025

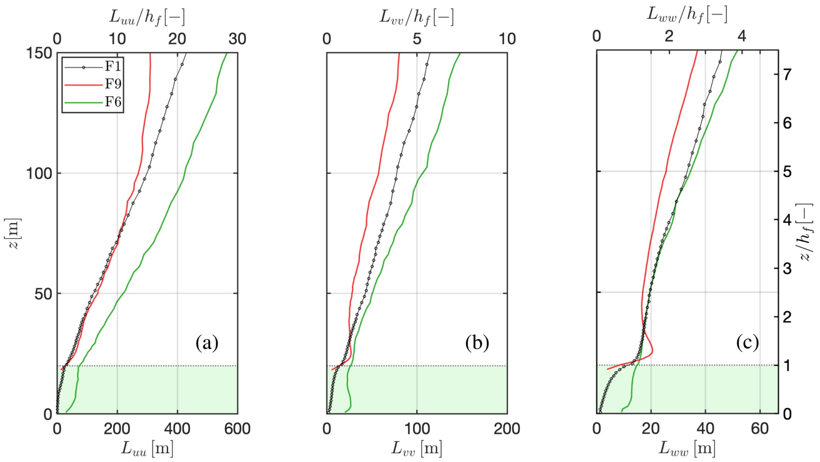

Figure 11. Integral lengthscales in the longitudinal, lateral and vertical directions. The markers on the curve of F1 indicate the location of cell centres, so they are indicative of the mesh resolution of all 3 cases. Note that x-axes show different ranges to highlight differences among cases.

forest density that are in line with the trends in skewness presented in the aforementioned works, namely the vertical decrease and increase in Sk_u, separated from around the mid-canopy and bounded between zero and 1.0. For Sk_w the trend mirrored on the negative side, although here the curves start closer to -1.0 than zero. The fall of Sk_u below zero near the ground for F1 is also displayed by some cases in the compilation of Raupach et al. (1996). Above the canopy, values get closer to zero with height pointing to a more symmetric shape in the probability distribution of wind and a more homogeneous turbulence.

Results for the Kurtosis in Fig. 13 align with the previous findings. The region inside the canopy and above it show larger values than the $K = 3$ of Gaussian distributions, implying the occurrence of strong wind events. While for K_u and K_v this corresponds to gusts, for K_w this equals to downwards sweeps. F1 shows peak values in the Kurtosis of all directions around the canopy, in contrast to F6 that displays a smoother progression from within the forest and upwards. Importantly, K_w for F6 is somewhat larger which supports the view of stronger downdrafts. Away from the forest region, velocity fluctuations become more uniform and $K \approx 3$. As a general note and to complement the previous remarks, the comparisons between the F1 and F6 agree with the trends in velocity, σ_u and σ_w (via k_{res}), integral lengthscales, Sk and K in function of increasing density as presented in the “family portrait" of (Raupach et al., 1996; Brunet, 2020).

https://doi.org/10.5194/wes-2025-114
Preprint. Discussion started: 14 July 2025

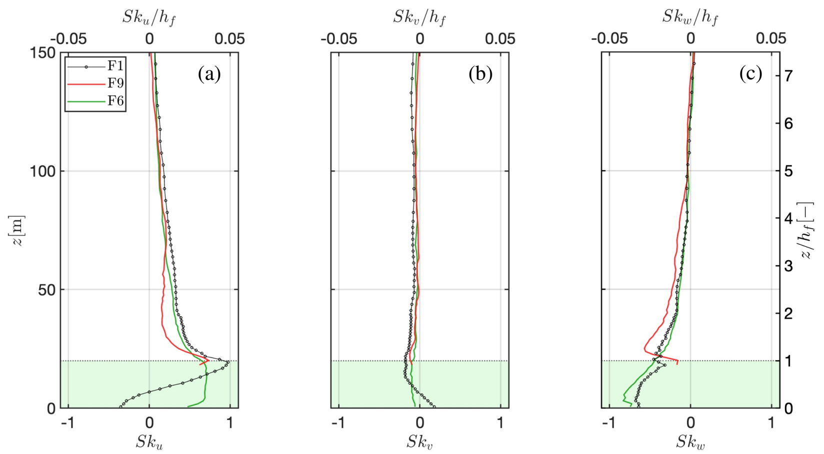

Figure 12. Skewness in the longitudinal (a), lateral (b) and vertical (c) directions.

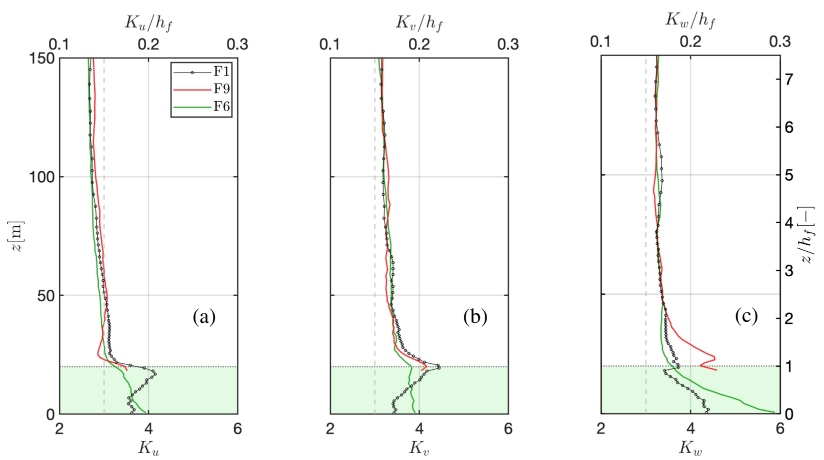

Figure 13. Kurtosis in the longitudinal (a), lateral (b) and vertical (c) directions. A vertical dashed line is included at $K = 3$.

https://doi.org/10.5194/wes-2025-114
Preprint. Discussion started: 14 July 2025

6.2 Wind flow comparison of LES and measurements

While the results in Section 6.1 present a verification of the method to model the forest impact on the flow aloft, this section presents a validation of the method using comparisons with tower measurements. The underlying research question is whether or not accuracy in the representation of the surface condition means that the model can accurately pick up differences in wind statistics from different wind directions. The evaluation is subjected to the constraint of statistical uncertainty, which is discussed in Sections 2.1 and 5.3.

To investigate the impact of upstream surface conditions on the wind at a hypothetical turbine location, a set of six simulations were performed. The first set consists of the three different wind directions used by Ivanell et al. (2018) referred to as R1, R2 and R3, simulated using as realistic elevation and PAD as possible, with the purpose of replicating the measured flow with maximum accuracy. The next set consists of 3 setups based on the 240° direction (R3), designed to investigate the relevance of employing accurate vegetation and elevation data as well as doing so over an extensive upstream region. These cases are built around the following premises:

- The region of realistic forest conditions is reduced to a small area of $5\,\mathrm{km} \times 5\,\mathrm{km}$ around the metmast. Outside this, the forest is homogeneous and represented with the average PAD. This is made in contrast to R3 that upstream of the metmast uses a realistic forest over $16\,\mathrm{km}+3\,\mathrm{km}$ in the *farm* (maximum resolution) and *transition* (cell stretching) areas, respectively. This case is named R3.1 .
- A domain that uses a realistic forest representation as in R3 but instead of the topographic variations, the domain surface is made flat. This case is called R3.2 .
- A domain that replaces the realistic forest representation by a uniform forest, with the average PAD, over the whole domain. This case is referred to as R3.3 .

The numerical setup of the cases is described in Sec. 4.2.3. The disposition of the terrain and forest in each case is presented in Table 3.

The wind speed and its shear, as represented by the shear exponent of the power law, is presented in Fig. 14. The wind speed is normalized with the 100 m TKE to facilitate comparison. From Fig. 14 (a) it is clear that the LES overpredicts the normalized wind speed, but that the relative differences between the directions follow the same trend as the measured wind profiles. It is also clear that the case R3.3, which was made with realistic elevation but homogeneous forest (using the average forest density and height), overpredicts the normalized wind speed and underpredicts the shear. These result are in line with theoretical expectations regarding the impact of heterogeneity of surface roughness, which says that unevenly distributed surface roughness leads to a higher effective roughness than when spread out evenly (Bou-Zeid et al., 2004, 2020; Janzon et al., 2023). As expected, R3, R3.1 and R3.2 are very similar close to the forest. R3 and R3.1 start to diverge slightly at 30 m height, but the difference remains small for the entire profile. It is interesting that the wind profile for R3.1 has lower values than R3 while R3.3 has considerably higher values, since for most of the domain, R3.1 and R3.3 have the same, constant, PAD and tree height. The difference is rather local and when the domain average wind speed is considered, both R3.1 and R3.3 shows larger

https://doi.org/10.5194/wes-2025-114
Preprint. Discussion started: 14 July 2025

WIND ENERGY SCIENCE DISCUSSIONS
Open Access

Table 3. Simulation cases for validation and footprint investigation. "Full" signifies that the representation of the real topographic variations extends over the complete domain surface. "Heterogeneous" refers to the detailed representation of the actual variability in tree height and leaf density. For case R3.1, The heterogeneous region has dimensions $\mathrm{L}_x = 3$ km + 2 km upstream and downstream, respectively, as well as $\mathrm{L}_y = 5$ km centred at the target position. Numerical setups are described in sections 4.2.2 and 4.2.3.

Case	Topography	Forest	Label
100° full	Full	Heterogeneous	R1
290° full	Full	Heterogeneous	R2
240° full	Full	Heterogeneous	R3
240° small forest	Full	Heterogeneous in metmast region, averaged PAD elsewhere	R3.1
240° flat	Flat	Heterogeneous	R3.2
240° homogeneous	Full	Average PAD	R3.3

wind speed and lower TKE than R3, as reported in Table 4. The domain averaged wind speed in R3.3 is 4.1 $\%$ larger at 100 m than in R3 and the resolved TKE 1.7 $\%$ lower which again illustrates that neglecting heterogeneity in the PAD leads to an underestimation of the effective roughness.

Table 4. Relative differences of the domain averaged quantities compared to simulation R3

Height	Wind speed			Resolved TKE			SGS-TKE		
	R3.1	R3.2	R3.3	R3.1	R3.2	R3.3	R3.1	R3.2	R3.3
25	0.201	0.176	-0.092	0.031	0.034	0.034	0.120	0.103	-0.149
40	0.123	0.109	0.022	-0.057	-0.050	0.075	-0.024	-0.026	0.022
100	0.062	0.055	0.041	-0.116	-0.103	-0.017	-0.081	-0.081	-0.005
140	0.047	0.042	0.030	-0.112	-0.099	-0.002	-0.083	-0.084	-0.008

For the higher order moments in Fig. 15, a notable observation is that the relatively coarse horizontal resolution of simulations R1-R3 has an impact on the anisotropy of the turbulence components. Relative to the measurements, the variance in u is overestimated while it is underestimated for v and w. Above 5 $\langle h_f \rangle$ the results agree better with the measurements. The case F1 employs a finer mesh that results in an anisotropy that better matches the observations below 5 $\langle h_f \rangle$. For the shear stress, the resolution seems to have a smaller effect and the simulations R1-R3 match the observations relatively well, accurately predicting that the magnitudes in 290° fall more quickly with height than in 100° and 240°.

For the skewness of velocity components in Fig. 16, the most distinct feature is the peak associated with the forest top, displaying a pattern of positive for u and negative for w indicative of sweep dominated mixing. Among the observations, which are only available at higher heights, the 290° shows the lowest values for the u-component and the highest for the w-

https://doi.org/10.5194/wes-2025-114
Preprint. Discussion started: 14 July 2025

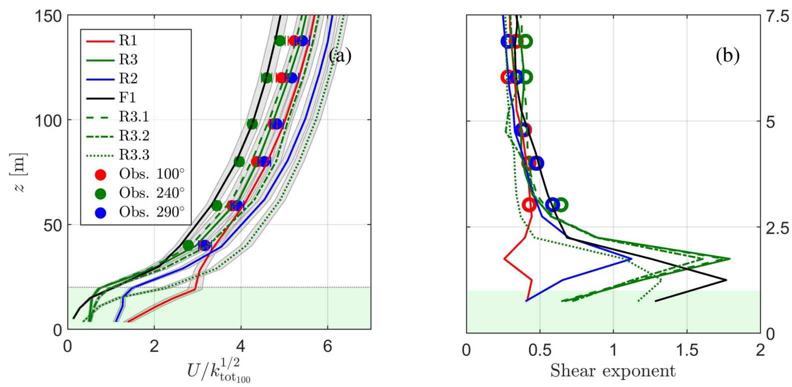

Figure 14. Wind profile (a) and wind shear exponent profile (b) from three wind directions for the tower position (Fig. 2). Lines represent the simulations in Table 3 as well as the reference case (F1 in Table 2). Measurements are indicated by circles with the estimation of 95 % statistical confidence for the mean values levels as errorbars. The green shaded area corresponds to forest height of $\langle h_f \rangle = 20$ m.

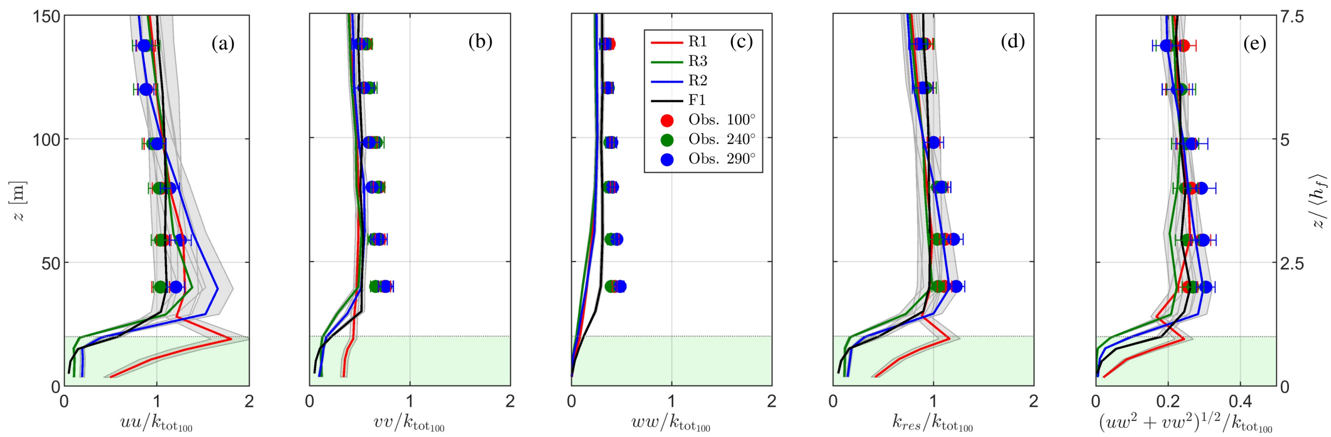

Figure 15. Second order turbulence moments normalized by the turbulence kinetic energy at 100 m height. Variance in the mean wind direction (a), lateral variance (b) vertical variance (c), resolved TKE (d) and total shear stress (e). Estimates for the statistical 95 % confidence levels of the mean values for the measurements are shown by the errorbars.

component, indicating a slightly more ejection dominated turbulence than the other two directions. While the magnitudes are different in the simulations the same trend is observed.

To further the discussion on the trade off between sufficient upstream fetch and sufficient resolution the simulations were also compared to observations in the frequency space. While it is evident the anisotropy is poorly represented below 100 m (Fig. 15) it is clear from Fig. 17 that the low frequencies agree with measurements for all three velocity components and that it is the relatively large share of variance that resides at high frequencies for v and w that leads to the poor agreements at low heights. The lower variance of case F1 compared to R1, R2 and R3 is also clearly evident. While the lack of forest

https://doi.org/10.5194/wes-2025-114
Preprint. Discussion started: 14 July 2025

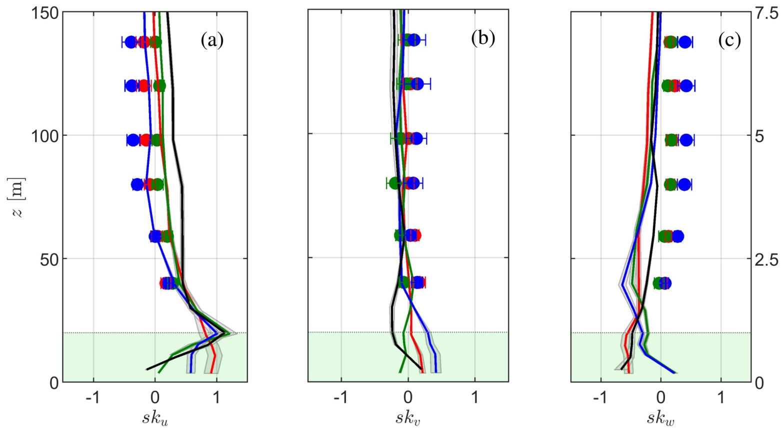

Figure 16. Skewness in the longitudinal, lateral and vertical directions for the 3 wind directions at Ryningsnäs.

heterogeneity in F1 contributes to the lower variance, most of the discrepancy comes from a lower geostrophic wind forcing. When studying cross-spectral densities, even at relatively small vertical separations and at heights well below the hub heights of modern turbines ($\delta_z = 18$ m separation, 91 m centre height), the agreement between observations and simulations is about equal on all frequencies (Fig. 18). For larger vertical separations, 40 m (Fig. 19) and 100 m (Fig. 20) the general level of coherence match between simulations and observations, as does the phase lag which is clear only for the v-component at 40 m separation but noticeable also for u at the larger separation. Notice that the frequency axis is scaled for the two-point spectral statistics to facilitate comparison with the F1 case.

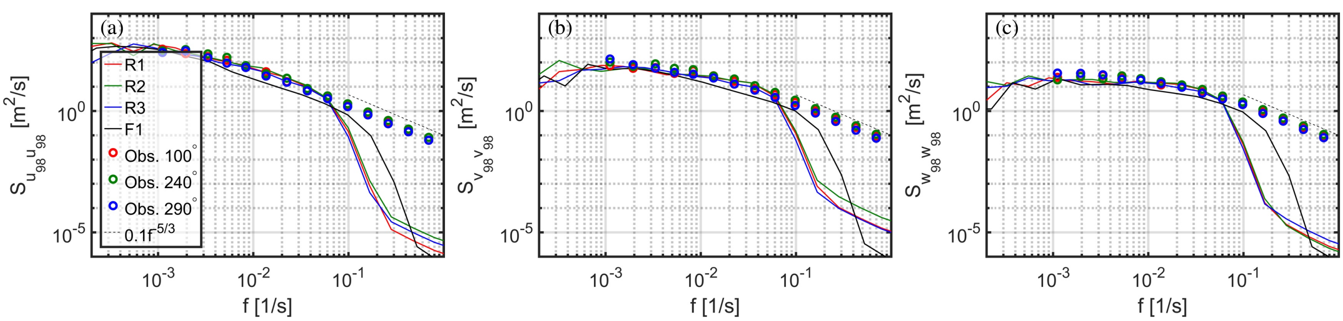

Figure 17. Power spectra of the longitudinal, (a), lateral, (b), and vertical, (c), velocity components at the height of 98 m.

https://doi.org/10.5194/wes-2025-114
Preprint. Discussion started: 14 July 2025

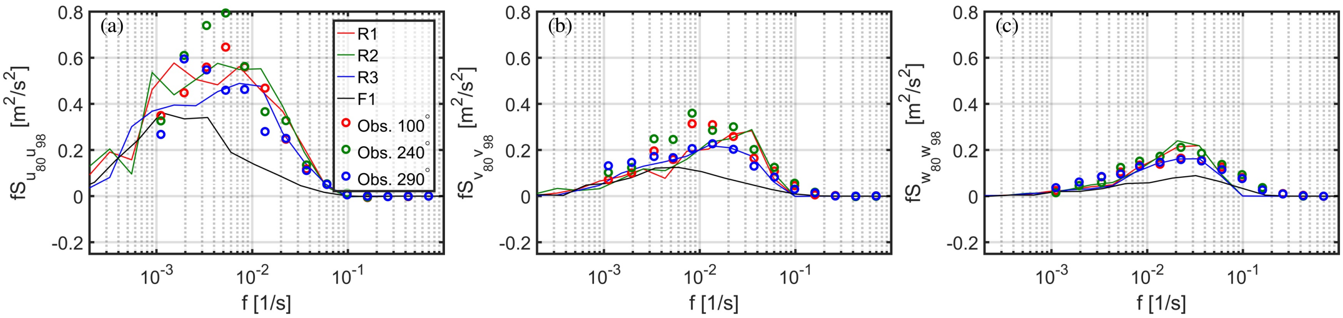

Figure 18. Vertical cross-spectra for $\delta_z = 18$ m separation of the longitudinal, (a), lateral, (b), and vertical, (c), velocity components.

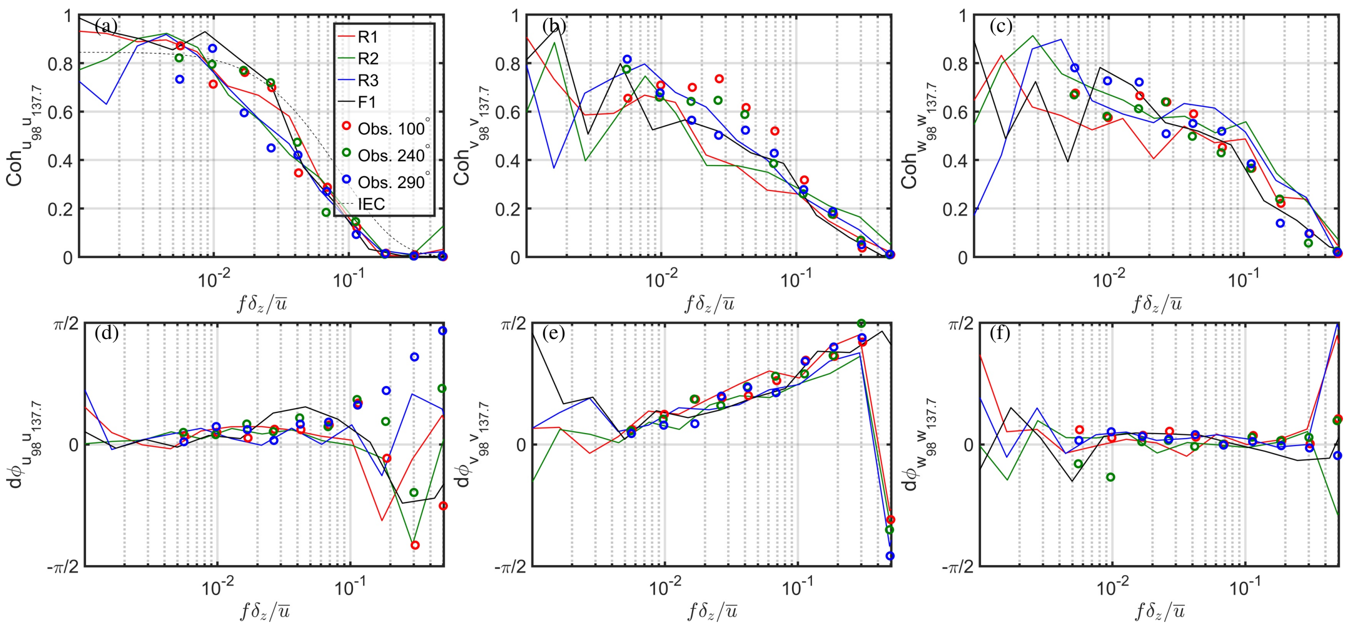

Figure 19. Coherence for $\delta_z \approx 40$ m separation of the longitudinal (a), lateral (b), and vertical (c), velocity components as well as phase shifts for the longitudinal (d), lateral (e), and vertical (f) velocity components as function of the normalized frequency.

https://doi.org/10.5194/wes-2025-114
Preprint. Discussion started: 14 July 2025

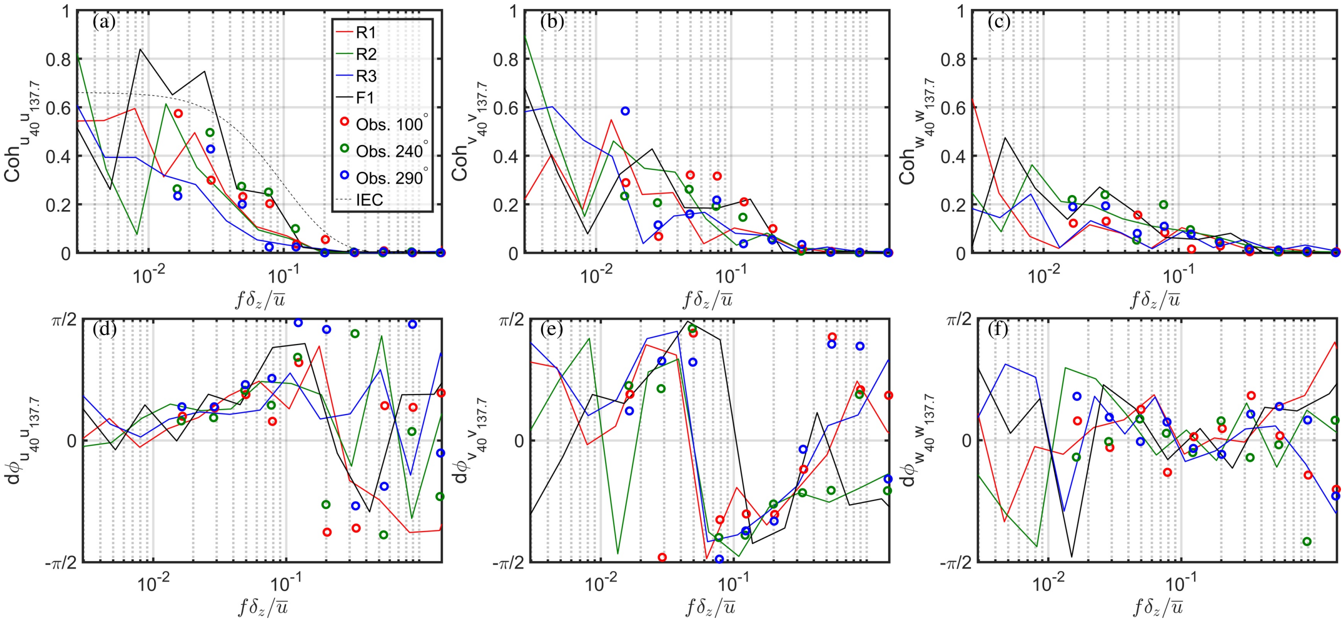

Figure 20. Coherence for $\delta_z \approx 100$ m separation of the longitudinal (a), lateral (b), and vertical (c), velocity components as well as phase shifts for the longitudinal (d), lateral (e), and vertical (f), velocity components as function of the normalized frequency.

https://doi.org/10.5194/wes-2025-114
Preprint. Discussion started: 14 July 2025

6.3 Footprint study

The focus is now placed on analyzing the impact of the forest modelling upstream of the metmast. Specifically, the significance of employing realistic forest conditions over an appropriate extension compared to using average forest values. The implications of using measured forest densities with all of its heterogeneity can clearly be seen in Fig. 14 (a) and (b), when focusing on the difference between case R3 and R3.3. The topography on those simulations is identical so the large difference in wind speed and shear is only due to the impact of the heterogeneity of the vegetation cover and density. The results agree with the findings of Bou-Zeid et al. (2004), Miller and Stoll (2013) and Janzon et al. (2023) which predict increasing effective roughness length with increasing surface roughness heterogeneity.

The R3.1 simulation was used to qualitatively assess the importance of using true vegetation cover in comparison with generic vegetation cover and the impact of limited upstream extent of true forest cover. Fig. 21 (a) and (b) shows the elevation and vegetation height of cases R3 and R3.1 whereas (c) – (f) shows the difference in normalized wind speed between the two simulations at heights 25, 40, 100 and 140 m above local ground, respectively. As expected, at 25 m height (just above the average forest height), the results reveal clear differences outside of the patch of equal PAD while within the region of equal PAD the wind speed is more alike, as illustrated by Fig. 21 (c). These variations are larger in regions devoid of trees in R3.0. At 40 m height, the patch of matching wind speeds have moved slightly downstream while the differences outside the region of equal PAD are smaller. At 100 m and above however, the influence of the equal-PAD region is hardly distinguishable and the maps are instead dominated by smaller differences in wind speed originating either from differences in upstream PAD or by impact from random fluctuations due to low frequency fluctuations.

The impact of the elevation induced speedup was qualitatively assessed in the same fashion by comparing wind fields from simulations R3 and R3.2 which share the same realistic forest cover, but where only R3 has realistic elevation and R3.2 is completely flat. The surface condition for R3.2 is showed in Fig. 22 (a), whereas the elevation of R3 is shown in Fig. 22 (b). When comparing normalized wind speeds above the local ground height for the two simulations, a speed up clearly appears that coincides with the terrain, as it is only present in R3 and not in R3.2. The speedup is most obvious at 40 and 100 m height. At 20 m height the pattern is dominated by small scale variations stemming from small scale terrain features, while at 140 m those are filtered out and only the larger terrain variations are visible in the speed-up pattern. Even though the speed-up pattern decreases in amplitude between 100 to 140 m above local ground, it is clear by comparing Fig. 22 (e) and (f) to Fig. 21 (e) and (f) that the pattern persists for much higher heights than the pattern linked to vegetation cover. It should be noted that a clear difference between the terrain-induced speed up pattern and the vegetation linked pattern is that the former stays horizontally consistent with increasing height, while the latter is somewhat advected downstream with height.

An extended perspective of the evolution of footprint with elevation is included in the Appendix. There, a comparison is made of the mean velocity, resolved and subgrid TKE from cases R3, R3.1, R3.2 and R3.3.

To quantitatively assess the requirements on domain size, the wind and TKE fields from simulations R1, R2, R3 and R3.2 were used. The wind fields where first normalized by removal of the mean and division by the standard deviation. The resulting fluctuations were then correlated with corresponding normalized fluctuations of surface drag, as measured by the magnitude

https://doi.org/10.5194/wes-2025-114
Preprint. Discussion started: 14 July 2025

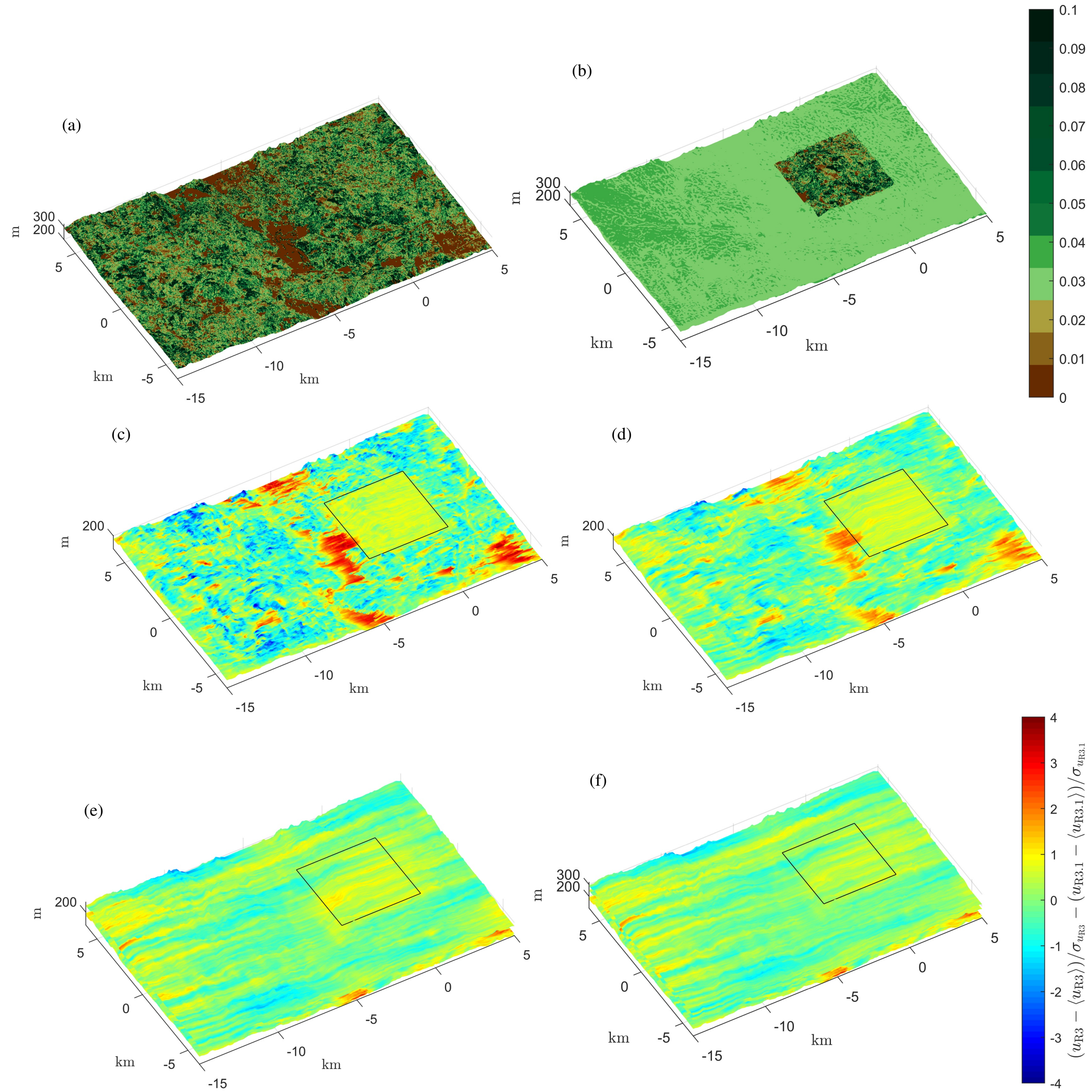

Figure 21. Vertically averaged PAD for runs R3 (a) and R3.1 (b). Difference between the normalized wind field fluctuations in case R3 and R3.1 at heights 25 m (c), 40 m (d), 100 m (e) and 140 m (f) above local ground level. Note that the vertical axis is exaggerated. A black square has been added to indicate the part of the domain coinciding with the region of realistic forest conditions in R3.1 .

https://doi.org/10.5194/wes-2025-114
Preprint. Discussion started: 14 July 2025

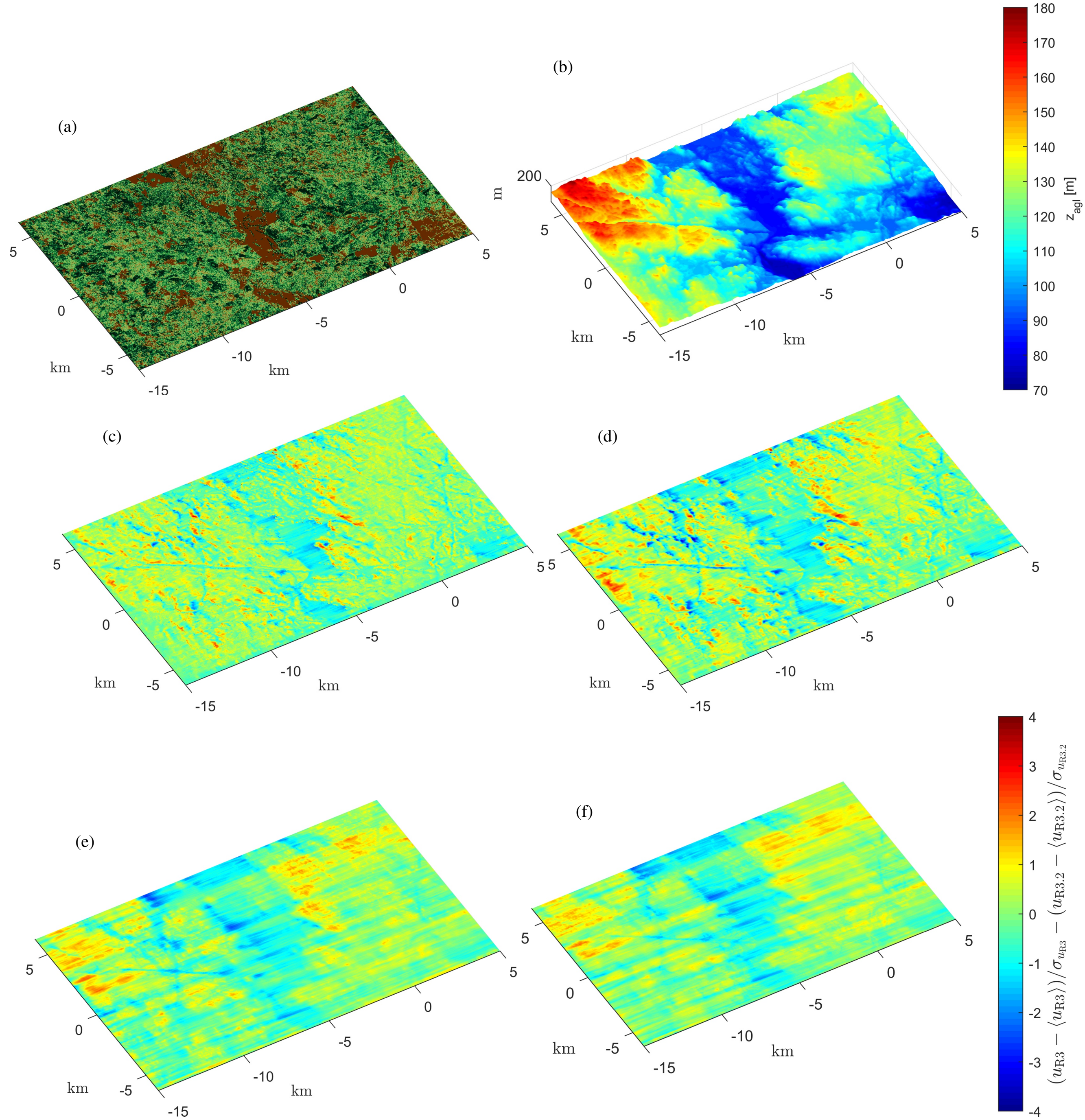

Figure 22. Surface conditions for runs R3.2 (a) and elevation in run R3 (b). Also, differences between the normalized wind field fluctuations in case R3 and R3.2 at heights 25 m (c), 40 m (d), 100 m (e) and 140 m (f) above local ground level. Note that the vertical axis is exaggerated.

https://doi.org/10.5194/wes-2025-114
Preprint. Discussion started: 14 July 2025

of the vertical integral of eq. (16). The correlation was made point-wise, starting with zero downstream separation and then varying the downstream separation while maintaining zero spanwise separation. The correlation was computed for all of the available 2-point pairs within the inner region of uniform meshing (see Fig. 2), meaning that less pairs were available with larger downstream separation (due to the finite extension of the domain). The results were similar when keeping the number of pairs constant, but plots using the maximum number of pairs are displayed here to reduce scatter. The results are shown in Fig. 23. For wind field fluctuations, two effects are distinguishable. At low heights and for small separation distances, the correlation is negative and comes from the fact that higher, denser vegetation leads to a local reduction in wind speed due to drag. The maximum impact of this effect is seen at roughly 4-10 times downstream z_{agl} as judged by the results in Fig. 23 (g) and (j). The second effect is seen at higher heights above the ground and appears to be connected to speed up due to varying displacement height. The correlation is positive, indicating that locally, higher drag somewhat counter-intuitively leads to a local increase in wind speed. For the resolved TKE an increase (decrease) in drag is associated to a increase (decrease) in TKE with the maximum located approximately 10 z_{agl} downstream. An exception is seen at 25 m height, which at smaller downstream distances than 10 z_{agl} has negative correlation. It is unclear whether this should be attributed to a spurious correlation between wind speed and TKE or whether it has to do with the model (in)ability to resolve small scale TKE. The subgrid TKE consistently shows a positive correlation with drag, again with a maximum effect roughly 10 z_{agl} downstream. The results from each simulation in Table 3 display very similar behaviour although it should be stressed that due to the terrain being flat in R3.2, this is the only case that is completely free of correlation between topography and forest height and thus the results from R3.2 should be more representative of the impact of surface drag. These considerations lead back to the requirements of domain size. From the results, there are no indications of a correlation between wind speed and surface properties that would extend much more than 10 z_{agl} upstream. Conversely, the correlation with drag and turbulence comprise greater distances, at least up to 50 z_{agl} upstream for rotor relevant heights, this will in turn have an impact on the local fluctuations as well as on the average wind speed.

6.4 Conclusions

This work has presented a methodology to simulate the wind field over forested regions that represent realistic conditions of topography and tree distribution. The methodology is based on LES and it permits to model the effect of the surface features on the turbulence characteristics of the flow. The surface characteristics comprise the representation of topography and crucially, the explicit representation of forest by means of a Plant Area Density (PAD) field so the drag on the wind flow is proportional to its local value as well as the flow velocity. The PAD and ground height can be determined trough airborne laser scans which has the great advantage that assumptions on roughness lengths and/or tree density profiles become much less important than in alternative approaches. The study has been divided into different parts whose conclusions are presented separately.

6.4.1 Verification

An extensive verification process has been shown, based on the simulation of idealized conditions comprising a homogeneous forest over flat terrain, that revealed the influence of various modelling choices in the flow characteristics. Attention was paid to

https://doi.org/10.5194/wes-2025-114
Preprint. Discussion started: 14 July 2025

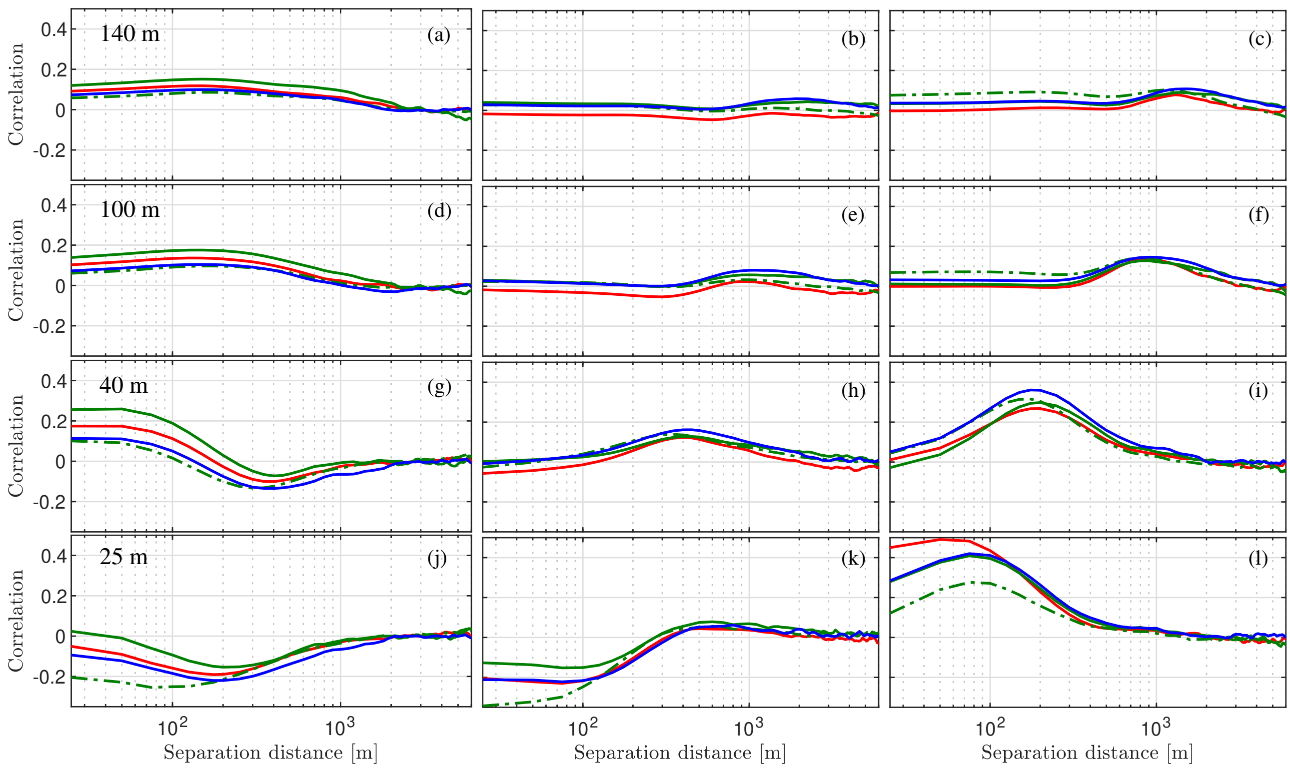

Figure 23. Domain average of the two-point correlation between the magnitude of the local forest drag with the velocity (left column), the resolved TKE (middle column), and the subgrid TKE (right column) as function of downstream separation between correlation pairs. The upper point in the correlation pair is at the height of 140 m (a), (b) and (c), 100 m (c), (d) and (f), 40 m (g), (h) and (i) and 25 m (j), (k) and (l) as indicated on the top left of each row. The lines follow the legend in Fig 14.

three cases, two with different PAD and one with only ground roughness z_0 and displacement height d. The turbulence statistics and spectra showed a general agreement with results found in the literature, while also confirming that the turbulence field above the forest is different when the forest is explicitly modelled in contrast to what is obtained when relying only on a wall model. Notably, higher streamwise skewness indicates a sweep dominated mixing above the modelled canopy. The verification also highlights the problem of achieving high enough turbulence based solely on large values of z_0, as this requires a minimum height of the first cell node above the ground and away the roughness sublayer to ensure the applicability of Monin-Obukhov (Basu and Lacser, 2017) while also maintaining a high cell resolution near this region. This problem does not appear when using PAD to model the forest drag. An important result of the verification is that in simulations employing PAD the z_0 value did not impact the mean statistics at wind turbine heights. In other words, drag from the canopy completely dominates over the drag from the surface, even when the PAD was set unrealistically low, showing no appreciable differences from when no wall model was used at all. The implication of this result is large, since on top of the issue with z_0 and the height of the first cell, PAD can be measured, but z_0 can not. Thus, using PAD eliminates the large uncertainty of estimating z_0 in the wind resource

https://doi.org/10.5194/wes-2025-114
Preprint. Discussion started: 14 July 2025

assessment, something that has been previously highlighted as an important challenge (Floors et al., 2018). An assessment of other modelling choices was also performed as part of the study. A significant result is that the flow characteristics at rotor heights were largely insensitive to the choice of subgrid-scale parametrization within the canopy, highlighting that the most important choice is between using a PAD field or not, whereas the details in the implementation of PAD drag only marginally impact the results at rotor heights, with changes being confined to the canopy level.

6.4.2 Validation

The methodology was validated by comparing the results of the simulation of wind flow over Ryningsnäs, a forested location with mild complex terrain located in Sweden. To represent the actual surface conditions, the technique makes use of detailed forest density and topography maps to create a PAD field in the simulation domain as well as ground surface with a high degree of accuracy. Three incoming wind directions were considered when comparing the LES results with observations, showcasing some variation in topographic and forest distribution. The methodology was shown to be able to represent the relative differences in velocity and shear as well as TKE. However, the general magnitude of the TKE was slightly underestimated and below 100 m the streamwise component had a positive bias, contrary to the lateral and vertical, an effect which is attributed to insufficient horizontal resolution similar to Arnqvist et al. (2019). Vertically separated spectral statistics generally agreed with measurements over various separation distances and heights, but the scatter in the data did not permit to show differences owing to upstream fetch, for either simulation or observations. Spectral coherence from the IEC model predicted higher values than both the LES and measurements for different separations δ_z as function of the normalized frequency $f\delta_z/\overline{u}$, a pattern that was also observed in the verification results under homogeneous forest conditions. While this result could suggest that the IEC model for spectral coherence might overestimate correlations outside the lowest frequencies under forested conditions, the cause could be more trivial. Indeed, if the velocity in the normalized frequency is not taken as the averaged value between the two locations as done here but a somewhat smaller value was used, the IEC curves would appear to shift towards smaller frequencies, providing a remarkable match to the LES results. To study what velocity would provide a better fit is left for future studies.

6.4.3 Capturing the footprint of the forest

Finally, a study of the footprint of the forest and topography was carried out with the aim of informing on the impact of surface conditions. The study examined the significance of representing forest heterogeneity by comparing results with those using a spatially uniform forest but identical topography. This showed that heterogeneous forest conditions not only produce a higher drag in comparison with homogeneous conditions, in agreement with prior studies (Bou-Zeid et al., 2020; Janzon et al., 2023), but also that accurately representing the forest indeed translates to better agreement with observations. Also the simulation with flat ground lacked in turbulence magnitude, but it should be noted that the studied site has low terrain complexity and that while realistic digital forest models may be difficult to acquire for all sites, realistic digital elevation models are much easier to find.

https://doi.org/10.5194/wes-2025-114
Preprint. Discussion started: 14 July 2025

Two-point correlations agree with initial assessment from scaling arguments that most of the footprint for velocity is within 10 times the height of interest. For turbulence, the footprint extended roughly five times longer. It should be emphasized that the simulations were run in strictly neutral conditions and a simulation in stable conditions, where the turbulence intensity is much smaller, would have a significantly longer footprint.

When comparing simulations using realistic forest in the entire domain to one where realistic forest is restricted to a small patch around the target location, the relative difference between the simulations showed no clear trace of the patch at a height above 100 m. The conclusion is that most of the difference is blended out and that remaining differences are seen only as a spatial mean quantities. In contrast, the usage of flat terrain in an otherwise identical representation of forest distribution indicated that differences observed in the wind field are more persistent with height. This is expected both because of terrain speed-up effects and because streamlines are not entirely terrain following, which leads to higher (lower) wind speeds at hills (depressions) in presence of a background wind shear.

6.4.4 Recommendations for site specific wind modelling

The validation supports the notion that the effect of surface features on the flow is fairly well represented in the computations. In addition, it also shows that the limited resolution of the mesh plays a role in the prediction of the anisotropy of second order quantities. The contrast between these findings offers the modeller two perspectives to weigh when it is desired to capture the footprint of the surface on the wind over long distances, in order to reproduce the wind characteristics seen at heights covered by the rotor area of a wind turbine. Other than single point anisotropy levels at low heights, no clear drawbacks were found from the relatively low resolution and since wind turbines will act as considerable spatial filters for turbulence, to employ domains that cover a sufficiently long region upstream of the metmast seems of greater importance compared to the refinement of the mesh, particularly in the horizontal direction.

The majority of the footprint for wind speed is located within 10 times the height of interest downstream, but is longer for turbulence. Since the effects of drag are both advected downstream and diffused by turbulence, the footprint is expected to be longer and narrower for stable conditions and sites with lower effective roughness. Missing heterogeneity in PAD leads to underestimation of the effective roughness, but using full heterogeneity only in the footprint did not increase the error relative to observations.

The simulations were made using periodic boundary conditions, which necessitate evening out the terrain at the edges of the domain. This should be considered when estimating the requirements on domain size since edge effects also advect and diffuse in the same manner downstream. Subsequently, if the manipulation of the terrain is large at the edges of the domain, an adjustment region before the footprint area should be included.

Finally, the most clear result was that using explicit forest drag instead of roughness and displacement makes the simulation less subjective and solves the problem of large z_0 relative to the first cell node z_1. The impact of particular choices in how to implement explicit drag were small compared to not using explicit drag at all.

https://doi.org/10.5194/wes-2025-114
Preprint. Discussion started: 14 July 2025

6.4.5 Directions for further research

All the simulations were made using strictly neutral conditions and the most obvious direction is to investigate the impact of atmospheric stratification. This will influence the extent of the footprint, but also change the effect of surface topography. How to treat the side boundary conditions have also been left out of this study and an interesting question is whether periodic boundary conditions are still viable when the terrain complexity is larger and if transient thermodynamic and pressure gradient forcing will be applied. While the PAD data certainly appear realistic, the effective roughness was slightly lower than for the tower observations. It remains an open question if this is due to a misrepresentation of PAD by the ALS-conversion technique, a resolution issue (either in PAD or the LES mesh) or if the problem is the treatment of the drag coefficient (either the magnitude or the use of a constant value).

Appendix

The following figures are shown to complement the view of the evolution of footprint discussed in Sec. 6.3. These provide a comparison of horizontal planes of mean velocity in Fig. A1, resolved TKE in Fig. A2 and subgrid TKE in Fig. A3, obtained at 25 m, 40 m, 100 m and 140 m above ground from setups R3, R3.1, R3.2 and R3.3 described in Sec. 4.2.3 and Table 3.

https://doi.org/10.5194/wes-2025-114
Preprint. Discussion started: 14 July 2025

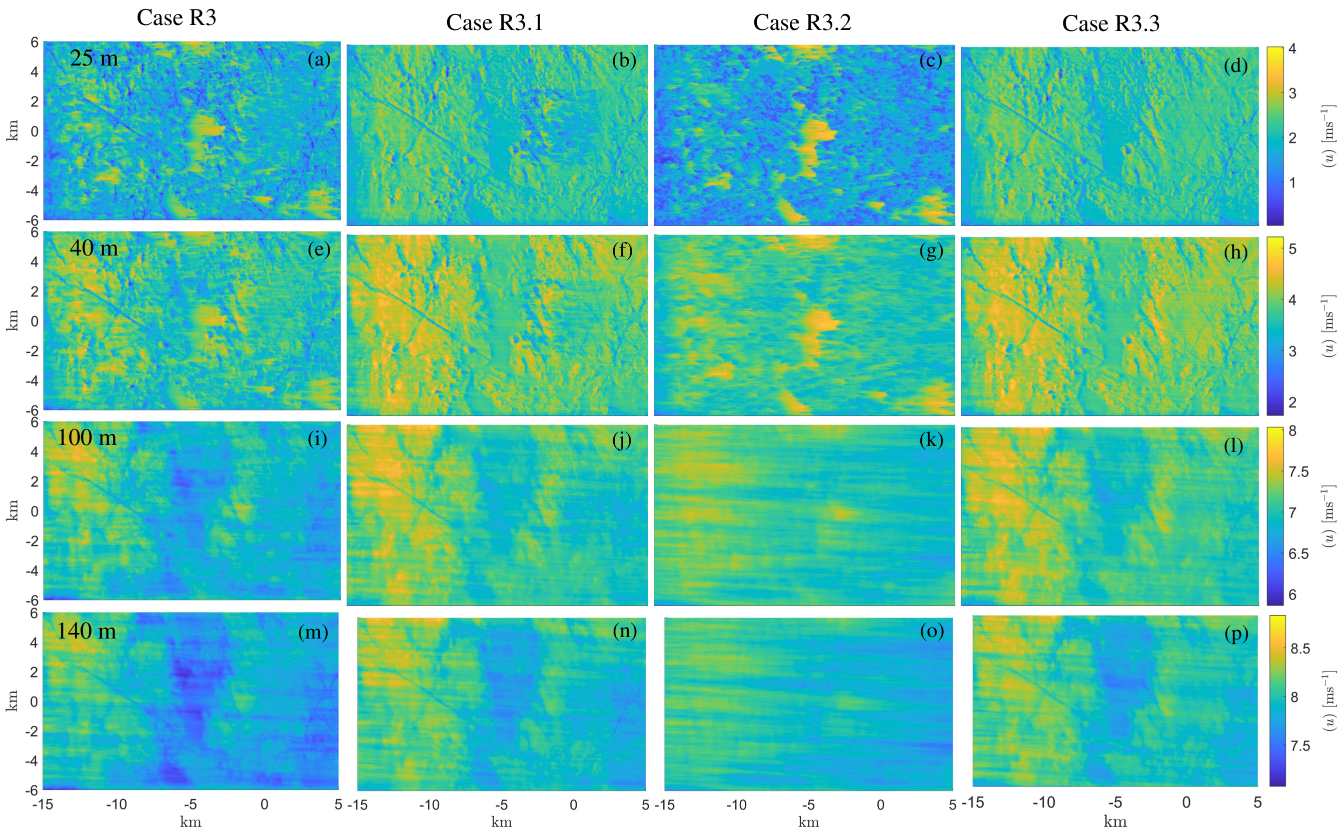

Figure A1. Temporal mean velocity fields at heights 25 m above local ground (a-d), 40 m above local ground (e-h), 100 m above local ground (j-l) and 140 m above local ground (m-p). Column 1 (a,e,i and m) is from simulation R3, Column 2 (b,f,j and n) is from simulation R3.1, Column 3 (c,g,k and o) is from simulation R3.2 and Column 4 (d,h,l and p) is from simulation R3.3 . Note that the scales vary for different elevations to highlight the features of the spatial distribution.

https://doi.org/10.5194/wes-2025-114
Preprint. Discussion started: 14 July 2025

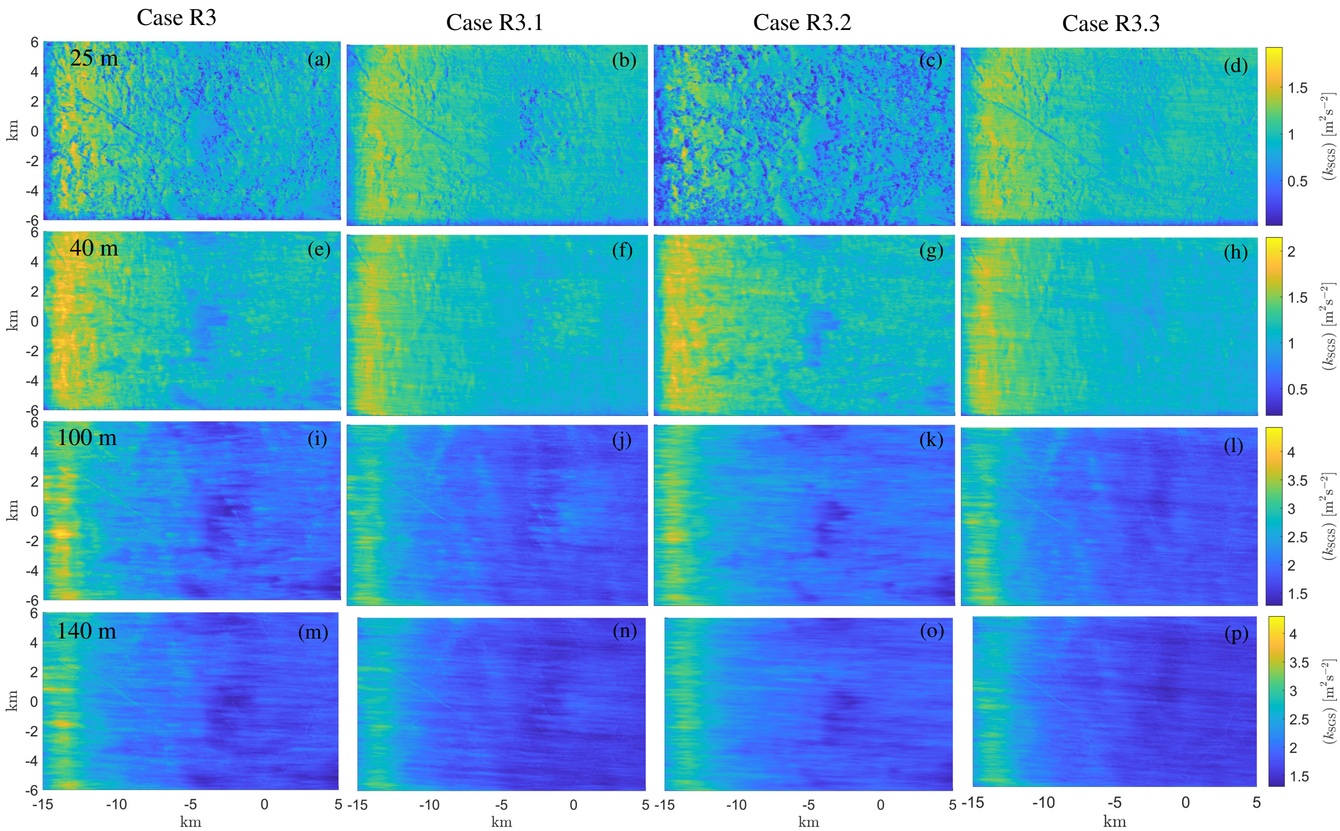

Figure A2. Temporal mean fields of the resolved TKE at heights 25 m above local ground (a-d), 40 m above local ground (e-h), 100 m above local ground (j-l) and 140 m above local ground (m-p). Column 1 (a,e,i and m) is from simulation R3, Column 2 (b,f,j and n) is from simulation R3.1, Column 3 (c,g,k and o) is from simulation R3.2 and Column 4 (d,h,l and p) is from simulation R3.3 . Note that the scales vary for different elevations to highlight the features of the spatial distribution.

https://doi.org/10.5194/wes-2025-114
Preprint. Discussion started: 14 July 2025

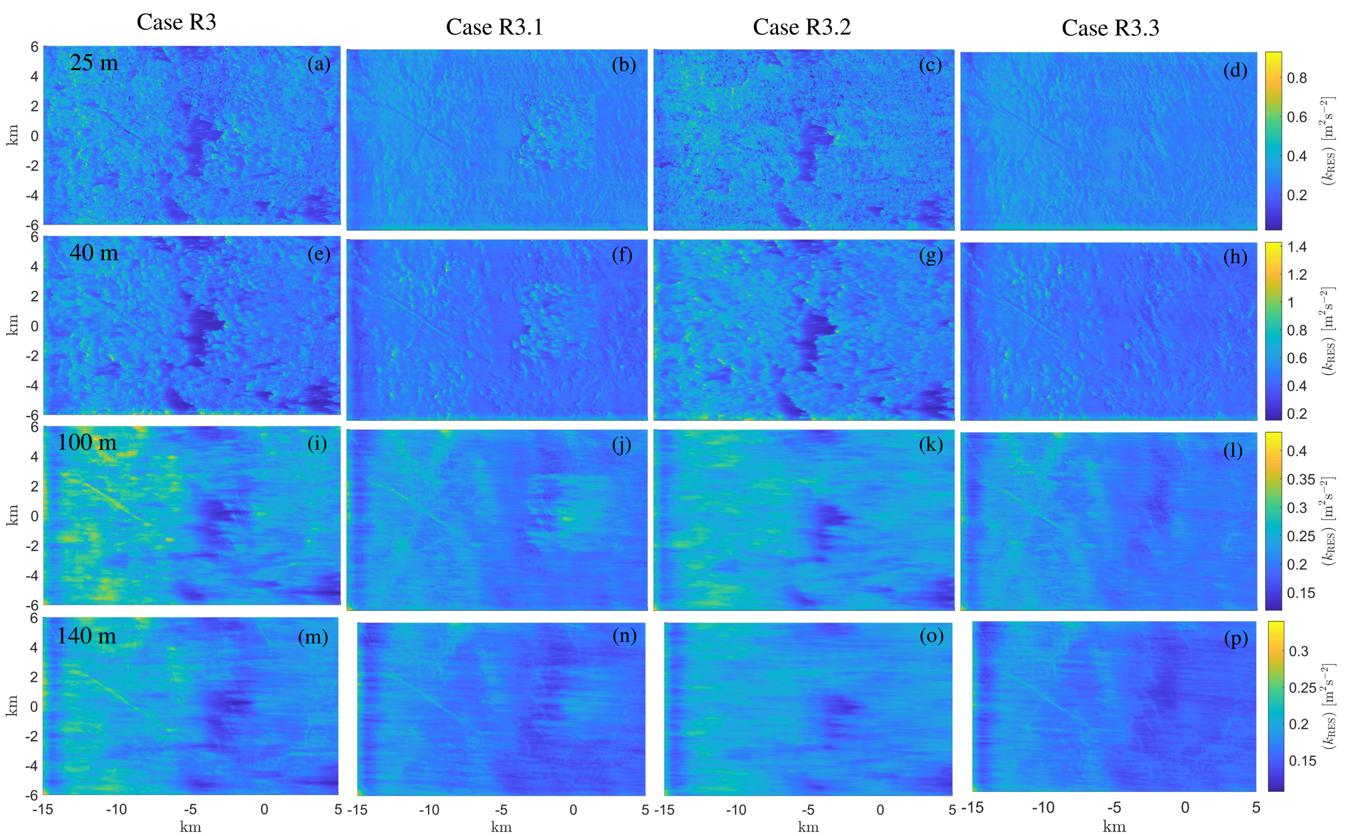

Figure A3. Temporal mean fields of the SGS-TKE at heights 25 m above local ground (a-d), 40 m above local ground (e-h), 100 m above local ground (j-l) and 140 m above local ground (m-p). Column 1 (a,e,i and m) is from simulation R3, Column 2 (b,f,j and n) is from simulation R3.1, Column 3 (c,g,k and o) is from simulation R3.2 and Column 4 (d,h,l and p) is from simulation R3.3 . Note that the scales vary for different elevations to highlight the features of the spatial distribution.

https://doi.org/10.5194/wes-2025-114
Preprint. Discussion started: 14 July 2025

Author contributions. Conceptualization and ideas: HOE and JA. Methodology development: HOE and JA. LES programming and implementation: HOE. Running the LES: HOE. Preparing measurement data and PAD field: JA. Data curation: HOE and JA. Verification: HOE with support by JA. Validation: JA with support by HOE. Visualization: HOE and JA. Writing (original draft preparation): HOE and JA. Writing (review and editing): HOE and JA.

Competing interests. The authors declare that they have no conflict of interest.

Acknowledgements. Funding for this work has been provided by the Energy Agency of Sweden under project number P2018-90109. This work was partly conducted within StandUp for Wind, a part of the StandUp for Energy strategic research framework in Sweden. The simulations were performed using resources provided by Swedish National Infrastructure for Computing (SNIC) and the National Academic Infrastructure for Supercomputing in Sweden (NAISS). The authors wish to thank Stefan Ivanell for his work as project coordinator and for his support.

References

Abedi, H., Sarkar, S., and Johansson, H.: Numerical modelling of neutral atmospheric boundary layer flow through heterogeneous forest canopies in complex terrain (a case study of a Swedish wind farm), Renewable Energy, 180, 806–828, 2021.

Adedipe, T. A., Chaudhari, A., and Kauranne, T.: Impact of different forest densities on atmospheric boundary-layer development and wind-turbine wake, Wind Energy, 23, 1165–1180, 2020.

Arnqvist, J., Segalini, A., and Dellwik, E.: Wind Statistics from a Forested Landscape, Boundary-Layer Meteorology, pp. 53–71, https://doi.org/10.1007/s10546-015-0016-x, 2015.

Arnqvist, J., Olivares-Espinosa, H., and Ivanell, S.: Investigation of Turbulence Accuracy When Modeling Wind in Realistic Forests Using LES, in: iTi Conference on Turbulence, pp. 291–296, Springer, 2019.

Arnqvist, J., Freier, J., and Dellwik, E.: Robust processing of airborne laser scans to plant area density profiles, Biogeosciences, 17, 5939–5952, 2020.

Arnqvist, J., Olivares-Espinosa, H., and Carlén, I.: Wind energy relevant characteristics of turbulence over boreal forests, in: Journal of Physics: Conference Series, vol. 2767, p. 092096, IOP Publishing, 2024.

Aumond, P., Masson, V., Lac, C., Gauvreau, B., Dupont, S., and Berengier, M.: Including the drag effects of canopies: real case large-eddy simulation studies, Boundary-layer meteorology, 146, 65–80, 2013.

Ayotte, K. W., Finnigan, J. J., and Raupach, M. R.: A second-order closure for neutrally stratified vegetative canopy flows, Boundary-Layer Meteorology, 90, 189–216, 1999.

Bailey, B. N. and Stoll, R.: The creation and evolution of coherent structures in plant canopy flows and their role in turbulent transport, Journal of Fluid Mechanics, 789, 425–460, 2016.

Basu, S. and Lacser, A.: A cautionary note on the use of Monin–Obukhov similarity theory in very high-resolution large-eddy simulations, Boundary-Layer Meteorology, 163, 351–355, 2017.

Bautista, M. C.: Turbulence modelling of the atmospheric boundary layer over complex topography, Ph.D. thesis, École de technologie supérieure, Montreal, Canada, 2015.

Bergström, H., Alfredsson, H., Arnqvist, J., Carlén, I., Dellwik, E., Fransson, J., Ganander, H., Mohr, M., Segalini, A., and Söderberg, S.: Wind power in forests: wind and effects on loads, 2013.

Bou-Zeid, E., Meneveau, C., and Parlange, M. B.: Large-eddy simulation of neutral atmospheric boundary layer flow over heterogeneous surfaces: Blending height and effective surface roughness, Water Resources Research, 40, 2004.

Bou-Zeid, E., Anderson, W., Katul, G. G., and Mahrt, L.: The persistent challenge of surface heterogeneity in boundary-layer meteorology: a review, Boundary-Layer Meteorology, 177, 227–245, 2020.

Boudreault, L.-É., Bechmann, A., Tarvainen, L., Klemedtsson, L., Shendryk, I., and Dellwik, E.: A LiDAR method of canopy structure retrieval for wind modeling of heterogeneous forests, Agricultural and forest meteorology, 201, 86–97, 2015.

Boudreault, L.-É., Dupont, S., Bechmann, A., and Dellwik, E.: How forest inhomogeneities affect the edge flow, Boundary-layer meteorology, 162, 375–400, 2017.

Brunet, Y.: Turbulent flow in plant canopies: historical perspective and overview, Boundary-Layer Meteorology, 177, 315–364, 2020.

Churchfield, M. J., Lee, S., and Moriarty, P. J.: Adding complex terrain and stable atmospheric condition capability to the OpenFOAM-based flow solver of the simulator for on/offshore wind farm applications (SOWFA), in: ITM Web of Conferences, vol. 2, EDP Sciences, 2014.

https://doi.org/10.5194/wes-2025-114
Preprint. Discussion started: 14 July 2025

Davenport, A. G.: The spectrum of horizontal gustiness near the ground in high winds, Quarterly Journal of the Royal Meteorological Society, 87, 194–211, 1961.

Dupont, S. and Brunet, Y.: Influence of foliar density profile on canopy flow: a large-eddy simulation study, Agricultural and forest meteorology, 148, 976–990, 2008a.

Dupont, S. and Brunet, Y.: Edge flow and canopy structure: a large-eddy simulation study, Boundary-Layer Meteorology, 126, 51–71, 2008b.

Dupont, S. and Brunet, Y.: Coherent structures in canopy edge flow: a large-eddy simulation study, Journal of Fluid Mechanics, 630, 93–128, 2009.

Dwyer, M. J., Patton, E. G., and Shaw, R. H.: Turbulent kinetic energy budgets from a large-eddy simulation of airflow above and within a forest canopy, Boundary-Layer Meteorology, 84, 23–43, 1997.

Finnigan, J.: Turbulence in plant canopies, Annual review of fluid mechanics, 32, 519–571, 2000.

Finnigan, J. J., Shaw, R. H., and Patton, E. G.: Turbulence structure above a vegetation canopy, Journal of Fluid Mechanics, 637, 387–424, 2009.

Floors, R., Enevoldsen, P., Davis, N., Arnqvist, J., and Dellwik, E.: From lidar scans to roughness maps for wind resource modelling in forested areas, Wind Energy Science, 3, 353–370, 2018.

Gancarski, P. and Chávez-Arroyo, R.: Meshing procedure for the atmospheric wind flow modelling, https://doi.org/10.5281/zenodo.1000490, 2017.

Gardiner, B. A.: Wind and wind forces in a plantation spruce forest, Boundary-Layer Meteorology, 67, 161–186, 1994.

Gavrilov, K., Accary, G., Morvan, D., Lyubimov, D., Méradji, S., and Bessonov, O.: Numerical simulation of coherent structures over plant canopy, Flow, turbulence and combustion, 86, 89–111, 2011.

Gavrilov, K., Morvan, D., Accary, G., Lyubimov, D., and Meradji, S.: Numerical simulation of coherent turbulent structures and of passive scalar dispersion in a canopy sub-layer, Computers & Fluids, 78, 54–62, 2013.

Greenshields, C.: OpenFOAM v3.0.1 User Guide, The OpenFOAM Foundation, London, UK, https://doc.cfd.direct/openfoam/user-guide-v3.0.1, 2015.

Högström, U.: Review of some basic characteristics of the atmospheric surface layer, Boundary-Layer Meteorology, 78, 215–246, 1996.

IEC: Wind energy generation systems - Part 1: Design requirements, Standard, International Electrotechnical Commission, Geneva, CH, 2019.

Ivanell, S., Arnqvist, J., Avila, M., Cavar, D., Chavez-Arroyo, R. A., Olivares-Espinosa, H., Peralta, C., Adib, J., and Witha, B.: Micro-scale model comparison (benchmark) at the moderately complex forested site Ryningsnäs, Wind Energy Science, 3, 929–946, https://doi.org/https://doi.org/10.5194/wes-3-929-2018, 2018.

Jackson, P.: On the displacement height in the logarithmic velocity profile, Journal of fluid mechanics, 111, 15–25, 1981.

Janzon, E., Arnqvist, J., Shapkalijevski, M., Körnich, H., and Rutgersson, A.: Modeling the Flow Response to Surface Heterogeneity during a Semi-Idealized Diurnal Cycle, Journal of Applied Meteorology and Climatology, 62, 511 – 527, https://doi.org/10.1175/JAMC-D-22-0063.1, 2023.

Kaimal, J. C. and Finnigan, J. J.: Atmospheric Boundary Layer Flows: Their Structure and Measurement, Oxford University Press, https://doi.org/10.1093/oso/9780195062397.001.0001, 1994.

Katul, G. G. and Chang, W.-h.: Principal length scales in second-order closure models for canopy turbulence, Journal of Applied Meteorology and Climatology, 38, 1631–1643, 1999.

https://doi.org/10.5194/wes-2025-114
Preprint. Discussion started: 14 July 2025

eawe european academy of wind energy
Open Access WIND ENERGY SCIENCE DISCUSSIONS

Kristensen, L. and Jensen, N.: Lateral coherence in isotropic turbulence and in the natural wind, Boundary-Layer Meteorology, 17, 353–373, 1979.

Lenschow, D. H., Mann, J., and Kristensen, L.: How Long Is Long Enough When Measuring Fluxes and Other Turbulence Statistics?, Journal of Atmospheric and Oceanic Technology, 11, 661 – 673, 1994.

Lu, S. and Willmarth, W.: Measurements of the structure of the Reynolds stress in a turbulent boundary layer, Journal of Fluid mechanics, 60, 481–511, 1973.

Lumley, J. and Panofsky, H.: The Structure of Atmospheric Turbulence, Interscience monographs and texts in physics and astronomy, Interscience Publishers, 1964.

Miller, N. E. and Stoll, R.: Surface heterogeneity effects on regional-scale fluxes in the stable boundary layer: Aerodynamic roughness length transitions, Boundary-layer meteorology, 149, 277–301, 2013.

Mohr, M., Arnqvist, J., Abedi, H., Alfredsson, H., Baltscheffsky, M., Bergström, H., Carlén, I., Davidson, L., Segalini, A., and Söderberg, S.: Wind power in forests II: Forest wind, 2018.

Niklas, K. J.: The aerodynamics of wind pollination, The Botanical Review, 51, 328–386, 1985.

Olivares-Espinosa, H., Arnqvist, J., and Ivanell, S.: Assessment of wind fields over forested sites with LES and a nacelle lidar, in: Journal of Physics: Conference Series, vol. 1256, p. 012002, IOP Publishing, 2019.

Pope, S. B.: Turbulent flows, Cambridge Univ press, Cambridge, United Kingdom, 2000.

Porté-Agel, F., Meneveau, C., and Parlange, M. B.: A scale-dependent dynamic model for large-eddy simulation: application to a neutral atmospheric boundary layer, Journal of Fluid Mechanics, 415, 261–284, 2000.

Raupach, M., Finnigan, J., and Brunet, Y.: Coherent eddies and turbulence in vegetation canopies: The mixing-layer analogy, Boundary-Layer Meteorology, 78, 351–382, 1996.

Robertson, A. N., Shaler, K., Sethuraman, L., and Jonkman, J.: Sensitivity analysis of the effect of wind characteristics and turbine properties on wind turbine loads, Wind Energy Science, 4, 479–513, 2019.

Sanz Rodrigo, J., Allaerts, D., Avila, M., Barcons, J., Cavar, D., Chávez Arroyo, R. A., Churchfield, M., Kosovic, B., Lundquist, J. K., Meyers, J., Muñoz Esparza, D., Palma, J. M. L. M., Tomaszewski, J. M., Troldborg, N., van der Laan, M. P., and Veiga Rodrigues, C.: Results of the GABLS3 diurnal-cycle benchmark for wind energy applications, in: Journal of Physics: Conference Series, vol. 854, p. 012037, IOP Publishing, 2017.

Sanz Rodrigo, J., Santos, P., Chávez Arroyo, R. A., Avila, M., Cavar, D., Lehmkuhl, O., Owen, H., Li, R., and Tromeur, E.: The ALEX17 diurnal cycles in complex terrain benchmark, in: Journal of Physics: Conference Series, vol. 1934, p. 012002, IOP Publishing, 2021.

Schindler, D., Bauhus, J., and Mayer, H.: Wind effects on trees, 2012.

Schumann, U.: Subgrid scale model for finite difference simulations of turbulent flows in plane channels and annuli, Journal of computational physics, 18, 376–404, 1975.

Shaw, R. H. and Patton, E. G.: Canopy element influences on resolved-and subgrid-scale energy within a large-eddy simulation, Agricultural and forest meteorology, 115, 5–17, 2003.

Shaw, R. H. and Schumann, U.: Large-eddy simulation of turbulent flow above and within a forest, Boundary-Layer Meteorology, 61, 47–64, 1992.

Silva Lopes, A., Palma, J. M. L. M., and Viana Lopes, J.: Improving a two-equation turbulence model for canopy flows using large-eddy simulation, Boundary-layer Meteorology, 149, 231–257, 2013.

https://doi.org/10.5194/wes-2025-114
Preprint. Discussion started: 14 July 2025

Silva Lopes, A., Palma, J. M. L. M., and Piomelli, U.: On the determination of effective aerodynamic roughness of surfaces with vegetation patches, Boundary-Layer Meteorology, 156, 113–130, 2015.

Sogachev, A.: A note on two-equation closure modelling of canopy flow, Boundary-layer meteorology, 130, 423–435, 2009.

Sogachev, A. and Panferov, O.: Modification of two-equation models to account for plant drag, Boundary-Layer Meteorology, 121, 229–266, 2006.

Sogachev, A., Kelly, M., and Leclerc, M. Y.: Consistent two-equation closure modelling for atmospheric research: buoyancy and vegetation implementations, Boundary-layer meteorology, 145, 307–327, 2012.

Su, H.-B., Shaw, R. H., Paw, K. T., Moeng, C.-H., and Sullivan, P. P.: Turbulent statistics of neutrally stratified flow within and above a sparse forest from large-eddy simulation and field observations, Boundary-Layer Meteorology, 88, 363–397, 1998.

Su, H.-B., Shaw, R. H., and Paw U, K. T.: Two-point correlation analysis of neutrally stratified flow within and above a forest from large-eddy simulation, Boundary-Layer Meteorology, 94, 423–460, 2000.

Svensson, U. and Häggkvist, K.: A two-equation turbulence model for canopy flows, Journal of wind engineering and industrial aerodynamics, 35, 201–211, 1990.

Thom, A.: Momentum absorption by vegetation, Quarterly Journal of the Royal Meteorological Society, 97, 414–428, 1971.

Weller, H. G., Tabor, G., Jasak, H., and Fureby, C.: A tensorial approach to computational continuum mechanics using object-oriented techniques, Computers in physics, 12, 620–631, 1998.

Wilson, N. R. and Shaw, R. H.: A higher order closure model for canopy flow, Journal of Applied Meteorology (1962-1982), 16, 1197–1205, 1977.

Wyngaard, J. C.: Turbulence in the Atmosphere, Cambridge University Press, https://doi.org/10.1017/CBO9780511840524, 2010.

Yoshizawa, A.: Statistical theory for compressible turbulent shear flows, with the application to subgrid modelling, The Physics of Fluids, 29, 1986.

Yoshizawa, A. and Horiuti, K.: A statistically-derived subgrid-scale kinetic energy model for the large-eddy simulation of turbulent flows, Journal of the Physical Society of Japan, 54, 2834–2839, 1985.

Zendehbad, M., Chokani, N., and Abhari, R. S.: Impact of forested fetch on energy yield and maintenance of wind turbines, Renewable energy, 96, 548–558, 2016.